

Electrochemical Ionic Synapses: Progress and Perspectives

Mantao Huang, Miranda Schwacke, Murat Onen, Jesús del Alamo,* Ju Li,*
and Bilge Yildiz*

Artificial neural networks based on crossbar arrays of analog programmable resistors can address the high energy challenge of conventional hardware in artificial intelligence applications. However, state-of-the-art two-terminal resistive switching devices based on conductive filament formation suffer from high variability and poor controllability. Electrochemical ionic synapses are three-terminal devices that operate by electrochemical and dynamic insertion/extraction of ions that control the electronic conductivity of a channel in a single solid-solution phase. They are promising candidates for programmable resistors in crossbar arrays because they have shown uniform and deterministic control of electronic conductivity based on ion doping, with very low energy consumption. Here, the desirable specifications of these programmable resistors are presented. Then, an overview of the current progress of devices based on Li^+ , O^{2-} , and H^+ ions and material systems is provided. Achieving nanosecond speed, low operation voltage (≈ 1 V), low energy consumption, with complementary metal–oxide–semiconductor compatibility all simultaneously remains a challenge. Toward this goal, a physical model of the device is constructed to provide guidelines for the desired material properties to overcome the remaining challenges. Finally, an outlook is provided, including strategies to advance materials toward the desirable properties and the future opportunities for electrochemical ionic synapses.

tions.^[1–3] However, the implementation of ANN using conventional hardware based on complementary metal–oxide–semiconductor (CMOS) circuits suffers from high energy consumption.^[4] The downscaling of physical feature sizes of CMOS transistors has been an effective approach to improve energy efficiency; however, there are concerns about potential slowdowns due to technological and economic challenges.^[5] As the data set size and model capacity grow exponentially,^[6,7] it is important to develop new architectures and hardware platforms that are energy efficient and suitable for bioplausible artificial intelligence algorithms.

Brain-inspired computing architecture based on crossbar arrays is a promising approach to performing ANN computations in the analog domain with high energy efficiency.^[8] In such crossbar arrays, the conductance of each device at the cross points represents the synaptic weights, which can be updated according to the desired learning rules. These analog

1. Introduction

Deep learning based on artificial neural networks (ANNs) has achieved outstanding performance in a wide range of applica-

crossbar arrays are intrinsically suitable for computations such as summation and product, so matrix–vector multiplication can be performed in parallel based on Kirchhoff's law and Ohm's law.^[9] Conventional von Neumann architecture separates memory and processing units, so frequent data transfers between the two consume a great deal of energy and create a bottleneck in logic-processor-centered computation. Crossbar arrays with programmable resistor elements colocate weight matrices and most matrix operations, hence reducing memory access and the related energy consumption.^[10] Indeed, the energy efficiency of computing architectures based on crossbar arrays is expected to be orders of magnitude better than that based on conventional digital hardware such as graphics processing units.^[11–13] An important research goal in the field is to develop devices with programmable resistances with the right characteristics related to energy consumption, speed, dynamics, and compatibility with nanofabrication.

While a variety of terms have been used in the literature to describe these cross-point elements, the most descriptive term for this main element of analog architectures is programmable resistors. At their core, their operation is relatively simple; that is, they have a conductance value that can be incrementally and bidirectionally tuned using electrical pulses of appropriate polarities (e.g., positive signals to increment and negative ones to decrement). In the absence of any

M. Huang, J. Li, B. Yildiz
Department of Nuclear Science and Engineering
Massachusetts Institute of Technology
Cambridge, MA 02139, USA
E-mail: lij@mit.edu; byildiz@mit.edu

M. Schwacke, J. Li, B. Yildiz
Department of Materials Science and Engineering
Massachusetts Institute of Technology
Cambridge, MA 02139, USA

M. Onen, J. del Alamo
Microsystems Technology Laboratories
Massachusetts Institute of Technology
Cambridge, MA 02139, USA
E-mail: alamo@mit.edu

 The ORCID identification number(s) for the author(s) of this article can be found under <https://doi.org/10.1002/adma.202205169>.

© 2023 The Authors. Advanced Materials published by Wiley-VCH GmbH. This is an open access article under the terms of the Creative Commons Attribution-NonCommercial License, which permits use, distribution and reproduction in any medium, provided the original work is properly cited and is not used for commercial purposes.

DOI: 10.1002/adma.202205169

signal, the device is expected to preserve its last programmed state.

Two-terminal resistive switching devices based on conductive filament formation or phase-change mechanisms are under intense investigation to realize cross-point elements. Such devices have small footprints and nanosecond switching speeds.^[9,14] However, the conductive filament mechanism is stochastic in nature, leading to high variability in analog resistive switching.^[15–17] Many efforts in engineering of materials, circuits, and programming have been made to ameliorate this variability issue, including confining the conductive filaments in preformed dislocations,^[18] implementing a dynamic voltage divider with series resistors to better control the switching voltage,^[19] and using a closed loop programming protocol,^[20] respectively. However, the variability challenge has not been fully addressed for practical applications, without sacrificing the area and energy efficiency, and the acceleration benefits. Alternatively, the phase-change mechanism has been associated with high energy consumption, drift, and abrupt decrement characteristics during amorphization.^[14,15,21] In order to train ANNs using analog crossbar arrays without degradation of accuracy, resistance modulation should be linear with respect to the number of programming pulses, symmetrical for opposite programming polarities, and reproducible from device to device and from cycle to cycle. Challenges remain for both types of mechanisms to achieve these desirable specifications.

Recently, electrochemical ionic synapses (EISs), also known as electrochemical random-access memory (ECRAM), with a three-terminal configuration have emerged as a new type of programmable resistor, based on a fundamentally different resistance modulation mechanism and structure. In the three-terminal configuration, the resistance of a channel is modulated by electrochemical ion and electron insertion into and extraction out of a conducting channel. The ion and electron insertion/extraction is controlled by the applied electrochemical potential at the gate terminal with respect to the channel layer. When the ions in use are small and mobile and their concentration in the active-channel material is in the random solid solution single-phase region of the phase diagram, the insertion/extraction under electric field is rapid across the channel area, and the final outcome does not significantly depend on the

microstructure of the channel. This gives rise to a deterministic, uniform, and highly repeatable modulation of the channel resistance; eliminating the stochasticity problem inherent to the two-terminal filamentary devices. These desirable characteristics have rendered EIS a promising candidate for implementing crossbar arrays for ANN accelerators and beyond. The concept has attracted strong interest and a wide variety of ions and material systems, including those based on Li^+ , O^{2-} , and H^+ are being investigated. Impressive progress has been made to improve device performance, reduce energy consumption, and improve linearity and symmetry.

As noted above, the EIS devices that we described here are also commonly referred to as ECRAM in the field. However, these devices are not random-access memories (RAMs). The EIS devices when applied in analog deep learning have a different set of expected characteristics compared to RAM, as we will discuss below in Section 3. Therefore, we choose to use “EIS” to refer to these devices, which describes both the operation mechanism and the function of such devices.

In this review, we first describe the principles of the electrochemical ionic synapse device operation, and present the desirable performance specifications in order for them to be applied in ANN computing. We then review different ion and material systems that have been explored to date in the realization of these devices and discuss the current progress and remaining challenges. We then construct a physical model of electrochemical ionic synapse devices based on an electrochemical equivalent circuit that includes ion transport and electrochemical reactions under an electric field. Simulations using this model provide insights into the dynamics of the device and also allow us to extract guidelines for the optimization of materials and interfaces to achieve the desired device specifications. Finally, we discuss the outlook for the development of electrochemical ionic synapses with improved performance to support the advancement of brain-inspired and neuroscience-guided computing systems.

2. Device Structure and Operation Principle

An EIS consists of three key functional layers: reservoir, electrolyte, and channel (Figure 1a). The reservoir stores ions

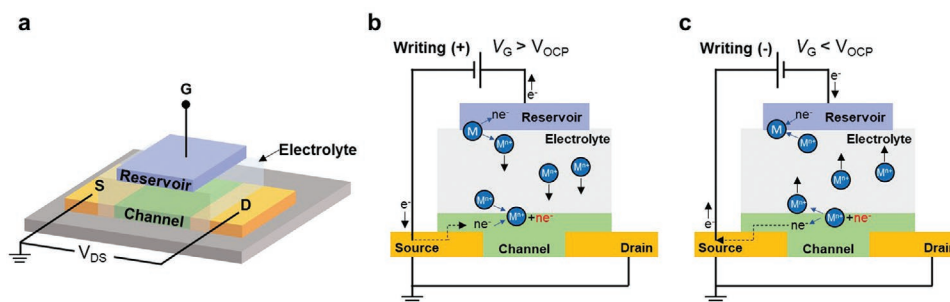


Figure 1. Device structure and operation principle of an electrochemical ionic synapse based on cation intercalation. a) Schematic illustration of the device. b,c) Schematic illustration of the writing process for an electrochemical ionic synapse based on cation transport (M^{n+}) and intercalation of M into the channel. b) A positive gate voltage (V_G) that is greater than the open-circuit potential (V_{OCP}) oxidizes the M species to form M^{n+} cations and extracts them from the reservoir. The cations M^{n+} migrate through electrolyte to the channel. The electrons follow the outer circuit and also reach the channel where they recombine to form M species. The M species donates its electrons (shown as ne^- in red) to available states which increases the electronic carrier concentration in the channel layer. c) A V_G that is lower than V_{OCP} reverses the processes in (b). Depending on the choice of mobile ions, the channel materials, and temperature, anions such as O^{2-} can also be transported through the electrolyte.

within, which are ready to be released upon the application of an electrical stimulus. The electrolyte, sandwiched between the reservoir and the channel, conducts ions (e.g., H^+ , Li^+ , O^{2-}) bidirectionally under an electric field while insulating electrons. The channel is made of materials with tunable electronic conductivity controlled by the ion concentration within. To operate the device, three conductive electrodes are placed: gate (G) contacting the reservoir, as well as source (S) and drain (D) contacting the two ends of the channel layer. The conductance of the channel can be read out by measuring the current from a small voltage (V_{DS}) applied across the source and drain. The first electrochemical ionic synapses were demonstrated by Thakoor et al. in 1990,^[22] and more recently, Fuller et al. proposed the application of EIS to physical artificial neural networks.^[23]

The mechanism for updating the weight of the electrochemical ionic synapse involves electronic conductance change of the channel layer, which is controlled by electrochemical ion and electron insertion. In a given neural network architecture, the channel layer itself serves as the synapse whose conductivity is controlled by the application of gate voltage on the EIS device. Upon application of voltage, $[M]_{channel}$ is controlled by dynamical electrochemical ion and electron transport from and to a reservoir $[M]_{reservoir}$ during service, mediated by an electrolyte layer for ion transfer and the outer circuit for electron transfer.

Figure 1b,c illustrates the conductivity modulation of the EIS at the channel layer, based on cation intercalation. The reservoir/electrolyte/channel construction is similar to a battery – a closed electrochemical system. A voltage applied to the gate (V_{GS} or V_G) controls the direction of ion movement in the electrolyte and the reactions at the electrodes. A positive gate voltage that is greater than the open-circuit potential (V_{OCP}) oxidizes the M species in the reservoir to form M^{n+} cations and extracts them from the reservoir. The cations M^{n+} are driven by the electric field to migrate through the electrolyte to the channel. The electrons follow the outer circuit and also reach the channel through the source contact. The electrolyte phase (ideally) does not conduct e^- , and conducts M^{n+} cations only, whereas the external electronic circuit conducts e^- only, and does not conduct M^{n+} . The channel is made of materials which are redox active, for example, transition metal oxides. The following autoionization reaction $M_{channel} \leftrightarrow M^{n+}_{channel} + ne^-_{channel}$ is possible within the solid-solution channel phase, giving the channel material its mixed ionic and electronic conductor character. A conductivity increase in the channel arises when the reconstituted M species donate their electrons to available states that can increase the electronic carrier concentration in the channel layer; for example, in-gap states of a transition metal in an oxide channel material. Conversely, a negative V_G reverses the process. The increase and decrease of the channel conductance are also referred to as potentiation and depression, respectively. At room temperature, the mobility of $e^-_{channel}$ or of the polaron on the reduced cation is many times larger than that of the ion, $M^{n+}_{channel}$. Therefore, with an increase of the dynamical dopant concentration in the channel, denoted as $[M]_{channel}$, the net electronic conductance of the channel increases. Also, since source and drain contacts (e.g., metallic Au) are “nonblocking” to $e^-_{channel}$ but are completely “blocking” to $M^{n+}_{channel}$, at steady-state read-out, only the conductance due to $e^-_{channel}$ contributes to the source-to-drain conductance. The

modulation of channel conductance from dynamical dopant concentration in the channel is similar to how boron or phosphorus dopants control the electronic conductivity of semiconducting Si, however with an important distinction: unlike $[B]_{Si}$ or $[P]_{Si}$ which is typically achieved by thermal diffusion or ion implantation during fabrication, $[M]_{channel}$ is controlled by dynamical electrochemical ion and electron transport from and to a reservoir $[M]_{reservoir}$ during service, mediated by an electrolyte layer for ion transfer and outer circuit for electron transfer. So $[M]_{channel}$ can change dynamically in service (aka dynamical dopants), throttled by electronic flow in the outer circuit, unlike $[B]_{Si}$ or $[P]_{Si}$ in conventional semiconductor electronics which stays fixed after the fabrication process.

Since the electrolyte blocks electronic conduction, and in the absence of any side reactions, all of the ionic charge flowing through the gate is transformed into intercalated or extracted dopants and/or a hybrid capacitive ion/electron accumulation at the interfaces. Opening the outside circuit after each voltage pulse blocks electron flow, and thus the backflow of ions, ensuring long-term retention and nonvolatility. Similar to the operation with cations, anions such as oxygen ions, O^{2-} , can also serve as the mobile ions; in this case, typically electrochemical oxygen extraction from a transition metal oxide layer increases electronic conductivity.

The rate of conductivity modulation depends on both the applied voltage, and on the intrinsic properties of the materials. The ion transport properties of the electrolyte, the charge transfer reactions for the “nonblocking” interfaces to M^{n+} (such as between the reservoir/electrolyte and the electrolyte/channel), and ion diffusion within the channel layer are key kinetic characteristics, and they can each limit the rate of writing the EIS in certain kinetic and size regimes that we will illustrate later.

The electrochemically controlled insertion/extraction of mobile ions in the lattice of the channel material is uniform across the entire gate stack and repeatable, in contrast to conducting filament forming mechanisms in two-terminal devices. The deterministic controllability of EIS, together with its energy efficiency and material and ion choices compatible with nanofabrication, makes them ideal candidates to be implemented into the crossbar arrays and other architectures for brain-inspired computing. Detailed resistance modulation mechanisms for different types of ions and channel materials, and performance to date will be presented in Section 4.

Compared to two-terminal resistive switching devices, which potentially offer cell area down to $4F^2$, where F is the minimum feature size of the fabrication process,^[24] three-terminal resistive switching devices generally need additional metal lines for operation, increasing the size of their minimum footprint. When assembled in crossbar arrays, electrochemical synapses are commonly proposed to be integrated with a transistor or a selector for alleviating the sneak path problem during programming. Alternatively, these additional devices can be avoided, if the EIS devices have a threshold modulation behavior, such that a half-bias selection scheme (i.e., coincidence detection) can be implemented.^[25] The EIS devices in a monolithically integrated circuit would be realized at the backend, where many of such devices would be layered (e.g., representing different matrices) on top of one another (with metal lines running between

successive layers). For a practical crossbar array, the array sizes get limited to $\approx 4000 \times 4000$ devices by the signal-to-noise ratio requirements, resistive line drops, and capacitive effects on pulse dispersion.^[25] Assuming devices are made smaller than $200 \times 200 \text{ nm}^2$, the bulk of the real estate would be occupied by the peripheral circuitry under these conditions. Those scales are easily achievable with both two- and three-terminal devices realized with conventional nanofabrication techniques and are already demonstrated in a recent work.^[26]

3. Desirable Specifications

Since one application of EIS is to serve as programmable resistor in analog deep learning architectures, we present below the desirable specifications of such devices in that context. Advances in materials and device structures for EIS should target these desirable specifications for high-performance deep learning.

Specifically, for analog deep learning applications, these devices are required to have many (10^2 – 10^3) nonvolatile conductance states, covering a large ($10\times$ – $20\times$) dynamic range.^[31] The former requirement allows these devices to accurately compute gradients with high resolution, whereas the latter ensures the states are separated enough such that the applied modulations are significantly larger than unwanted changes such as thermal noise. In reality, the EIS devices have analog tunability, discretized at the level of an individual ion. The definition of number of states is the average number of pulses that one would need to change the conductance value of a device across the full range. The range 10^2 – 10^3 states was generated following a series of empirical simulation studies for a variety of neural network types that achieved minimal error penalty compared to using floating points.^[25,28,29] Recent works have introduced new methods that reduce those numbers all the way down to ≈ 20 .^[30] Moreover, the minimum resistance of these devices is also required to be high (that is, $\gtrsim 1$ – $5 \text{ M}\Omega$ at the potentiated state) such that a large-scale array (e.g., 1000×1000) can be achieved without suffering from the voltage drop in the metal lines as well as minimizing the overall energy consumption.^[25]

Most importantly, the modulation behavior in between these states should be symmetric, meaning a unit decrement pulse should be able to undo the effect of a unit increment pulse at any given conductance level.^[11,25,28] In addition to many empirical observations,^[8,11,25,28,31–33] it was also theoretically shown that device asymmetry is fundamentally incompatible with conventional neural network training algorithms, as it distorts the energy landscape in a manner the optimization process cannot handle.^[34] We can quantify symmetry using the asymmetry ratio defined by Nikam et al.^[35]

$$AR = \left[\frac{\max |G_p|(n) - \max |G_d|(n)}{G_{p(100)} - G_{d(100)}} \right] \text{ for } n = 1 - 100 \quad (1)$$

where $|G_p|$ and $|G_d|$ are the average conductance values during potentiation and depotentiation, respectively, and $G_{p(100)}$ and $G_{d(100)}$ are the conductance values after 100 potentiation or depotentiation pulses. For an ideal device, $AR = 0$.

The linearity of the channel conductance as a function of the number of pulses is often discussed in the EIS literature. Here,

we use the definition of linearity provided by Jang et al.^[36] which gives the conductance of the channel G as

$$G = \begin{cases} ((G_{LRS}^\alpha - G_{HRS}^\alpha) \times w + G_{HRS}^\alpha)^{1/\alpha} & \text{if } \alpha \neq 0 \\ G_{HRS} \times (G_{LRS}/G_{HRS})^w & \text{if } \alpha = 0 \end{cases} \quad (2)$$

where G_{LRS} and G_{HRS} are the conductance of the channel in the low-resistance state and high-resistance state, respectively, w is an internal variable which increases with the number of pulses, and α is a nonlinearity factor which can refer to potentiation (α_p) or depotentiation (α_d). For a perfectly linear and symmetric device $\alpha_p = \alpha_d = 1$.

An often-overlooked requirement for these devices is that, under the application of a half-amplitude programming signal (also called a half-selected device), the conductance needs to remain practically unchanged. This requirement can be satisfied either with the intrinsic nonlinear voltage response of the EIS device or with the integration of a selector device with each EIS. This property is crucial to be able to implement the fully parallel update method shown in refs.^[25,28,32]

For analog deep learning operations, these devices also need to have very high endurance as well as good retention characteristics. Considering that training operations comprise very high numbers ($>10^{10}$) of small incremental modifications, materials used in programmable resistor technologies need to maintain their properties throughout many cycles over long durations.

As for retention, the change in channel conductance due to any unintended accumulating effects needs to be sufficiently small compared to the intentional modulations exerted by the algorithm. Roughly speaking, as long as the time constants for those unintended effects are slower than the time it takes to train the network for an epoch, the algorithm should be able to counteract them without trouble. On the other hand, for inference applications, the retention metrics are much more critical and are required to be many orders of magnitude longer than those for training applications. From a material perspective, this presents a critical design choice since long retention often contradicts with fast and low-energy modulation characteristics.^[37] We note that, in EIS, nonvolatile retention is ensured by opening the circuit that blocks electron flow, and consequently the backflow of the ions. Thus, co-optimization of speed and nonvolatility is possible.

The programming voltages of these devices need to be compatible with standard integrated circuit drivers, which suggests operation under $\approx 1 \text{ V}$.^[10,25] Programming with 1 V or less is also desirable for energy efficiency of the devices.

The programming voltage needs to be higher than the OCP as discussed in Section 2, so low operation voltage requires a small OCP. It is possible to achieve zero OCP, for example, by using the same material for both the channel and the reservoir with the same ion concentration in the initial state. In addition to a small OCP, a weak dependence of OCP on the conductance state would be beneficial for maintaining a consistent change of conductance per pulse over different initial conductance states at low operation voltages.^[38] Devices with small change of OCP could be achieved if the conductivity of the channel material is highly sensitive to a small amount of ion intercalation. WO_3 is a potential candidate material for low

OCP change, as Yao et al. reported that the conductance can be changed by >4 orders of magnitude with a small change of OCP (≈ 40 mV) at low hydrogen concentrations for $x = 0-0.05$ in H_xWO_3 .^[39] The channel material Li_xTiO_2 also showed only a small change (70 mV) in OCP while doubling the conductance of the channel, and over $10\times$ channel conductance change during phase transformation at constant OCP.^[38]

In addition to the requirements given above for the devices to be functional, the device modulation needs to be fast and energy efficient, such that the analog processors can indeed provide acceleration benefits while also reducing the overall power consumption. The devices are expected to change a single-state worth of conductance by the application of pulses shorter than 10 ns.^[25] Multiple pulses may be sent to the same devices with intervals comparable to the pulse duration. After the pulse application, the channel conductance may continue to rise, and stabilize after a delay that is longer than the pulse duration. Ideally, the conductance change should stabilize within ≈ 300 ns after the pulse (i.e., which is approximately the time between processing successive inputs using backpropagation),^[25] so that the full conductance change can be read out in the next inference round. In a fully pipelined operation (i.e., all arrays operating at any given time), each device would always be used under forward-backward-update subcycles. The forward and backward cycles (the same operation) are limited by the signal-to-noise ratio of the array. In this estimation, we assumed each would take 100 ns.^[25] A design where each subcycle takes the same time simplifies the scheduling, which is why update is also assumed to take 100 ns. Therefore, we suggested that the previous update cycle should preferably finalize before the next one starts. To better estimate how critical a delayed modulation would be under a learning task, further simulation studies would be needed.

The energy efficiency of artificial intelligence (AI) training and simulations must be improved by more than 1000 000-fold,^[40] based on the exponentially increasing computing energy demand projections into the following few decades. Ideally, the energy consumption of the artificial synaptic device should be close to, or even better than the biological synapse, which consumes 1–100 fJ per synaptic process.^[41,42] The energy consumption of the devices is characterized by integrating the instantaneous current multiplied by the instantaneous voltage that is supplied to the gate over the pulse duration. Note that simply multiplying the static power consumption by the pulse duration yields incorrect energy consumption values ignoring losses due to displacement currents evolving during the transients. If extra components such as transistors are integrated with the synapses, the energy consumption from the extra components also need separate considerations. Fast modulation dynamics provide the key acceleration benefit of analog deep learning processors, whereas low energy consumption decreases the cost of operating such architectures as well as increases the attainable device density. Analog-digital conversions, nonlinear activation function computations, and communications between crossbar arrays and with external systems will also contribute to the energy consumption of the whole system. These peripheral computations and communications may consume a comparable or greater amount of energy than the crossbar arrays.^[25] Energy efficiency

improvements could be made by codesign and co-optimization of the entire system with the EIS devices.

Any programmable resistor technology aiming to realize practical analog processors must build on top of standard logic CMOS and therefore must rely on CMOS-compatible materials and involve back-end-of-line (BEOL)-compatible processes. This implies a maximum fabrication process temperature of 400 °C. Moreover, the device operation should not rely on unconventional environmental conditions such as high temperature or humidity.

In order to be able to achieve high device density in such chips, the total device footprint needs to be less than 200×200 nm²^[25] and should be fabricated on multiple levels, stacked at the backend. The device area and power consumption metrics often disallow implementing additional circuitry around the analog devices, to compensate for their intrinsic nonidealities.

4. Material Systems for Electrochemical Synapses

In the search for EIS device designs that meet the aforementioned requirements, a variety of material systems and working ions have been investigated. Many early devices were based on the movement of Li^+ ions through materials that have been originally developed for battery applications, including lithium phosphorous oxynitride (LiPON) and lithium perchlorate ($LiClO_4$) polymer electrolytes and $LiCoO_2$ and WO_3 cathodes. However, a major disadvantage of Li-based devices is that Li is not compatible with CMOS processing. Alternatively, CMOS-compatible O^{2-} -based devices have also been investigated. These devices generally use a WO_x channel material, paired with yttria-stabilized zirconia (ZrO_2)_{1-x}(Y_2O_3)_x (YSZ) or HfO_2 electrolyte. Nevertheless, due to the large size and double valency of the O^{2-} ion, these devices often operate at too high voltages and consume too much energy for efficient training of neural networks or rely on heating to enable faster movement of the O^{2-} ion. As both a CMOS-compatible and an energy-efficient option, the smallest ion, H^+ has also been investigated as the working ion. While some H^+ -based devices rely on polymer electrolytes and organic channel materials, such as Nafion and poly(3,4-ethylenedioxythiophene):poly(styrene sulfonate) (PEDOT:PSS), there are recent reports of all-inorganic devices using WO_3 as the channel and SiO_2 -based electrolytes which are compatible with CMOS processing. Some researchers have also investigated integrating 2D materials into the EIS device, either as the channel or an additional ionic sieve between the channel and electrolyte to prevent the buildup of ions at the interface. We present a review of progress and remaining challenges in each of these categories in the following sections.

4.1. Lithium-Ion-Based

The first demonstration of an all-solid-state, three-terminal, nonvolatile EIS device using Li^+ ion was reported by Fuller et al. in 2016, as shown in **Figure 2a**.^[23] While electrochemical transistors which showed volatile changes in channel conductance from the field-induced movement of ions had been previously reported,^[36,43–45] Fuller et al.'s device differed by the

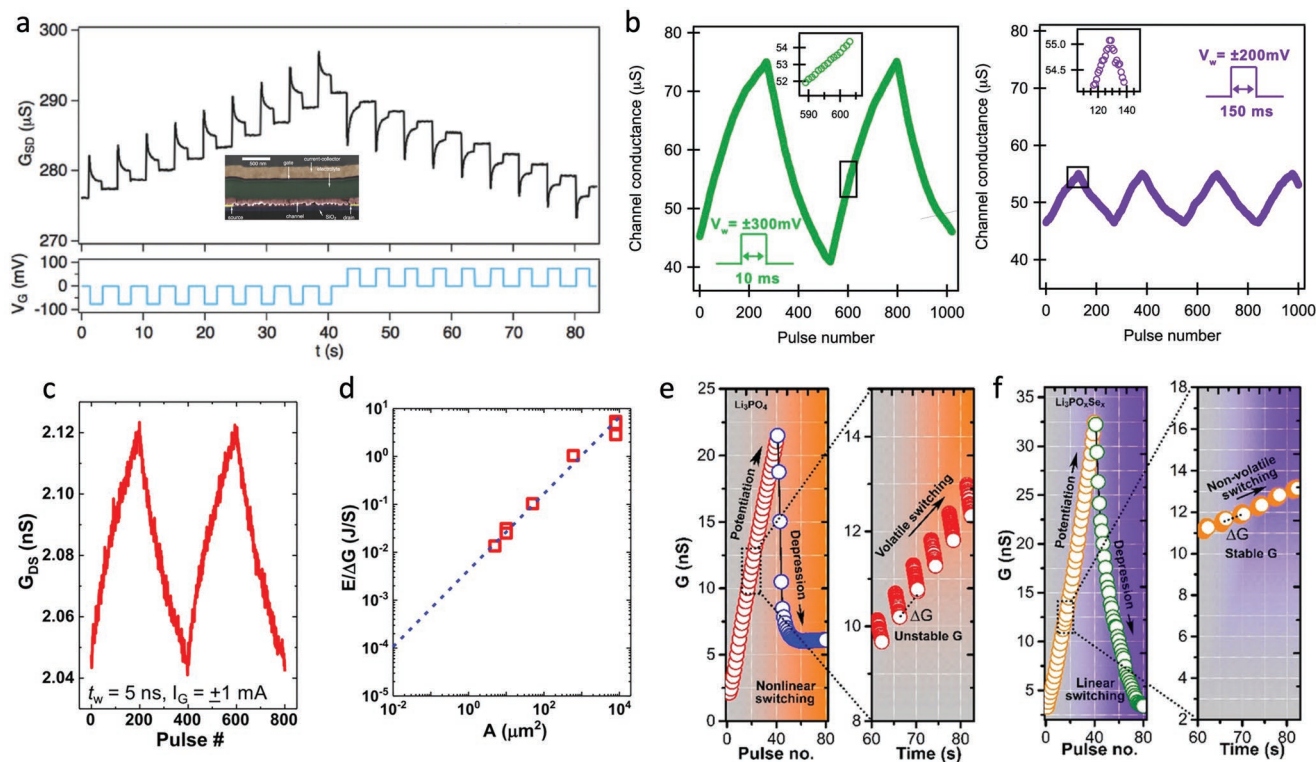


Figure 2. Summary of progress in Li-based devices. a) Channel conductance during constant voltage pulsing of original EIS device reported by Fuller et al. Inset shows false-color scanning electron microscopy (SEM) image of device cross-section. Adapted with permission.^[23] Copyright 2016, Wiley-VCH. b) Channel conductance updates of symmetric EIS design paired with diffusive memristor developed by Li et al. which allows for operating voltages as low as ± 300 and ± 200 mV. Adapted with permission.^[38] Copyright 2019, American Chemical Society. c) Tang et al. showed reproducible cycling of devices with 5 ns pulses ($I_G = \pm 1$ mA), where the total pulse period is 1.5 s. d) Tang et al. also showed that write energy per conductance change scales linearly with device area, assuming an average gate voltage of 1 V. Adapted with permission.^[46] Copyright 2018, IEEE. e,f) Nikam et al. showed that the use of (e) low Li-ion conductivity Li_3PO_4 electrolyte yields devices with volatile and nonlinear conductance states, while use of (f) high-conductivity $\text{Li}_3\text{PO}_{4-x}\text{Se}_x$ electrolyte yields state-of-the-art devices with nonvolatile and linear states. Adapted under the terms of the CC-BY Creative Commons Attribution 4.0 International license (<https://creativecommons.org/licenses/by/4.0/>).^[47] Copyright 2019, The Authors, published by Springer Nature.

addition of an electrolyte between the gate and channel, so that in the absence of an applied bias, dopants cannot diffuse out of the channel as there is no source of electrons to allow for their reduction. Fuller et al. referred to their devices as Li-ion synaptic transistor for analog computation (LISTA), a type of nonvolatile redox transistor.

The LISTA consisted of a Si gate electrode, 400 nm thick LiPON electrolyte, and 120 nm thick $\text{Li}_{1-x}\text{CoO}_2$ channel where the channel length is 2 μm . With constant current gating ($|I_G| = 350$ nA), Fuller et al. tuned the conductance of their channel between 4.5 and 270 μS , which also changed the OCP from 0 to -4.2 V. Nearly identical performance is observed across 4 LISTA devices. The retention and endurance of the devices are promising, with programmed conductance states being maintained for several weeks, and no degradation in performance being observed after 40 cycles (traversing an average of 200 states each) varying OCPs between -3.0 and -4.1 V. In search of a regime where linear updates are possible, Fuller et al. found that in the range $G_0 = 180\text{--}230$ μS , ΔG versus G_0 is nearly constant, with a linear slope of $\approx 2.5 \times 10^{-3}$ for current gating ($|I_G| = 200$ nA) and $\approx 3.5 \times 10^{-3}$ for voltage gating ($|V_G| = 15$ mV). While ΔG is confirmed to scale linearly with pulse amplitude and length down to 1 ms, for shorter pulses,

the response is limited by diffusion of Li in the channel. This slowness is a major disadvantage for these devices. Fuller et al. asserted that improving the crystallinity of $\text{Li}_{1-x}\text{CoO}_2$ could increase the diffusivity by a factor of 10^3 . This would put the modulation speed in the microsecond range, which is still not fast enough as described in Section 3. Nevertheless, Fuller et al. did project a very low energy consumption for the movement of ions in their devices ($E = QV$), <10 aJ per write operation for 0.04 μm^2 device area.

The use of lithium ions in EIS devices has many advantages. As the second smallest ion, Li^+ has high mobilities in solids, which is promising for designing devices with fast modulation and low energy consumption. Furthermore, materials with high Li^+ diffusivity have been thoroughly investigated for battery applications, providing a good starting point for choosing materials for EIS devices. For these reasons, EISs based on Li^+ ion intercalation into inorganic channels have been widely studied since the publication of Fuller et al.'s work.^[23,38,46–49]

Common channel materials being studied are Li_xWO_3 and LiCoO_2 . In these materials, Li acts as dopant and contributes free electrons into WO_x , MoO_3 ,^[48] and holes into LiNiO_x , LiTiO_x ,^[50] and therefore changes the electronic conductivity of the channel. Alternatively, deintercalation of Li from LiCoO_2

oxidizes Co from 3⁺ to 4⁺ and causes an insulator–metal transition (IMT), changing the conductivity by a factor of 10⁶.^[51,52] Li_{1-x}CoO₂ is an attractive channel material as intercalation of Li ions only weakly strains the lattice for $x < 0.5$, and Li diffusion has a low activation energy at 0.25 eV.^[23] WO₃ is a well-known electrochromic material, frequently used in smart windows. Intercalation of small ions like H⁺ and Li⁺ into amorphous or polycrystalline WO₃ causes it to undergo an IMT and to change from transparent to dark blue.^[53] For lithium in particular, the electrical resistivity of Li_xWO₃ decreases dramatically, over four orders of magnitude, as x is increased between $0 < x < 0.1$. For $x > 0.1$, the electrical resistivity of Li_xWO₃ continues to decrease but more gradually, with the IMT occurring for $0.2 < x < 0.24$. This change in resistivity is driven by an increasing number of electrons in the W 5d states.^[54] Furthermore, Li_xWO₃ is known to have several phase transitions; it is monoclinic for $x < 0.01$, tetragonal for $0.08 < x < 0.12$, and cubic for $x > 0.36$.^[54]

Regarding Li_xTiO₂, for $x < 0.2$, there exists the tetragonal anatase solid solution, while $x > 0.4$ corresponds to orthorhombic Li-titanate solid solution; for $0.2 < x < 0.4$, there is a two-phase coexistence regime of the anatase and Li-titanate phases.^[38,55] While remaining in the anatase phase ($x < 0.2$), it is found that a 70 mV change in OCP as Li is inserted corresponds to approximately doubling the conductance of the channel.^[38] However, in the two-phase regime ($0.2 < x < 0.4$), the conductance sharply decreases as Li is inserted, resulting from the phase transition to Li-titanate which has strong electron–electron correlations. The same 70 mV OCP change results in a 10× change in channel conductance. Once the single-phase Li-titanate phase regime ($x > 0.4$) has been reached, the channel conductance begins to increase again with increasing concentration of Li in Li_xTiO₂. While the two-phase region is attractive in that much wider conductance ranges are achievable with the same write voltage, phase transformations in Li_xTiO₂ have long equilibrium times, such that the channel takes ≈1 min to relax to a steady state, far too long for practical applications of EIS. The two-phase/voltage plateau regions of faster battery electrodes like Li_xFePO₄ and Li_{4+3x}Ti₅O₁₂ may be more promising for fast, low-voltage EIS.^[38]

The range of conductance which is achievable in a given channel material is also important, as many devices that have been reported operated at too high of a conductance range for practical applications. Modification of device dimensions could allow for tuning of the channel conductance range to some extent. However, the ratio of $W:L$ can only practically be modified by a factor of about three, and changing the thickness of the channel could impact the uniformity of dopants in the channel and modulation transients. Some authors have succeeded in operating Li-based EIS devices based on WO₃^[46] and LiCoO₂^[47] channels in the nanosiemens conductance regime. However, Li_xTiO₂ has only been shown to operate in the micro-siemens conductance regime.^[38]

LiPON is often used as the solid-state electrolyte for Li-based EIS devices. LiPON has shown bulk ionic conductivity on the order of 3×10^{-6} S cm⁻¹ at room temperature.^[56] LiPON also has a large chemical stability window and high electrical resistivity.^[23] Furthermore, LiPON layers as thin as 15 nm deposited by reactive sputtering maintain good ionic conductivity (1×10^{-6} S cm⁻¹) and high electronic resistivity (10^{15} Ω cm).^[57] In

LiPON, doping with N atoms increases the Li-ion conductivity by an order of magnitude compared to Li₃PO₄. Similarly, the substitution of the O atoms in Li₃PO₄ with less electronegative Se can reduce the electrostatic interactions between Li atoms and the lattice, reducing the Li-ion migration barrier from 0.3 to 0.253 eV, and increasing Li-ion conductivity to 2×10^{-6} S cm⁻¹. Li₃PO_{4-x}Se_x has been successfully implemented in Li-based EIS devices.^[47] Like LiPON, Li₃PO_{4-x}Se_x can be deposited from a Li₃PO₄ target, with Se flux from a Se target as opposed to flowing N₂ gas.^[47] Solid-state polymer electrolyte polyethylene oxide (PEO):LiClO₄ has also been successfully used in EIS devices due to the high Li-ion conductivity in PEO. However, PEO:LiClO₄ is soluble in common lithographic solvents, which makes scalable fabrication of the top gate challenging. Therefore, most devices using this electrolyte are fabricated in a lateral geometry, where the gate is separated by at least several micrometers from the channel.^[47]

Si was first used as the gate reservoir material for exploration,^[23] but the cell has a wide OCP range (0–4.2 V). This may prevent low voltage operation and affect linearity under constant voltage gating. Unlike energy consumption, the OCP does not scale with the area of devices and is largely determined by the thermodynamics and reaction kinetics of the material system. The implementation of alternative anode materials or symmetric cells can be used to reduce the OCP. To achieve low OCP values, Li et al. created a symmetric device with Li_xTiO₂ ($0 < x < 0.65$) as both the channel and the gate reservoir materials, separated by solid polymer electrolyte LiClO₄ in PEO.^[38] With this symmetric structure, in the initial state where both gate and channels have the same Li concentration ($x \approx 0.1$), the OCP is 0 V. As Li is moved between the gate and channel, leading to a <5% change in x and doubling in channel conductance from 40 to 80 μS, the OCP changes by only ≈70 mV. This allows for low write voltages ($|V_{\text{gl}}| = 200\text{--}300$ mV), shown in Figure 2b, compared to most Li-based EIS devices ($|V_{\text{gl}}| = 1\text{--}3$ V).

Many of the channel and electrolyte layers for Li⁺-based EIS, including WO₃, LiCoO₂, and LiPON, are grown by radio frequency magnetron sputtering.^[23,39] These materials are also compatible with conventional lithography techniques, and are stable at temperatures above 400 °C. However, regardless of the CMOS compatibility of the methods used to fabricate Li-based EIS devices, the Li ion itself can contaminate Si substrates and devices. This issue could be resolved by developing Li diffusion barriers such as TiN.^[58,59]

While most reported Li-based EIS devices have channel lengths on the order of micrometers, Tang et al. have reported scaling of their LiPON/WO₃ devices down to 300×300 nm² area.^[46] Compared to larger devices, this scaled device maintained discrete conductance states and good retention and had an even larger on/off ratio (10^3 compared to 40 for 10×60 μm² devices). However, the linearity is decreased in the scaled device. Figure 2c shows that Tang et al. were able to program their devices with write pulses down to $t_w = 5$ ns where the conductance level of the channel is read 1.5 s after each pulse.^[46] Furthermore, they confirm that the average change in conductance per pulse ΔG scales linearly with write pulse width between $t_w = 5\text{--}400$ ns as expected for a charge-driven programming mechanism given the linear relationship between pulse charge Q and write pulse width ($Q = I_G \times t_w$). Based on the

pulse width and dimensional scaling, Tang et al. projected for their LiPON/WO₃ material system, 100 × 100 nm² devices with $t_w = 1$ ns and $\Delta G = 0.01$ nS would consume 1 fJ per write event (Figure 2d), matching the energy consumption of synaptic events in the human brain. It is unclear whether this energy calculation accounts for the electrostatic CV² contribution.

Nonlinearity in Li-based EIS has been investigated by Nikam et al. They observed nonlinear conductance updates in devices based on Li⁺ intercalation into WO₃ through a LiClO₄/polyvinyl alcohol (PVA) polymer solid electrolyte.^[35] They attributed the nonlinear behavior to the tendency of Li⁺ to diffuse into WO₃, leading to a large flux of Li⁺ ions into WO₃ during a few initial pulses and the formation of a dense Li⁺ ion cluster at the electrolyte–channel interface that is reduced to a Li dendrite, stopping further insertion of Li⁺ ions into the channel. Devices that incorporate a layer of graphene between the electrolyte and channel avoid the formation of Li dendrites due to stabilization of the interface and the moderate barrier to Li⁺ ion movement through graphene. Nikam et al. found that devices with a graphene layer have much-improved linearity, symmetry, and nonvolatility.^[35]

Nikam et al. reported another strategy for improving both the linearity and symmetry of updates by improving ionic transport through the electrolyte.^[47] They fabricated two types of EIS devices with LiCoO₂ as the channel material, one using Li₃PO₄ as the electrolyte and another using Li₃PO_{4-x}Se_x. They found that for the Li₃PO₄ device, the conductance states are volatile and updates are extremely nonlinear for depotentiation, as shown in Figure 2e. Nikam et al. hypothesized that due to the low ionic conductivity of Li₃PO₄, Li extracted from the channel during potentiation accumulates at the channel/electrolyte interface, where it can diffuse easily back into the channel during the read periods or during depotentiation. Meanwhile, the Li₃PO_{4-x}Se_x device with %Se content = 0.26 shows non-volatile modulation (Figure 2f), attributed to the fast Li-ionic conductivity in this electrolyte. This device also shows state-of-the-art symmetry (AR = 0.12) and linearity ($\alpha_p/\alpha_d = 1.33/-0.34$). Interestingly, they also found that with lower Se content (%Se content = 0.13), there is still a good deal of nonlinearity with both potentiation and depotentiation curves being concave up, once again due to low electrolyte ionic conductivity. However, for higher Se content (%Se content = 0.52), the conductance update curves have the “shark tooth” shape commonly seen with EIS devices when the channel conductance becomes saturated. Nikam et al. attributed this to the formation of a barrier layer by unreacted Se.

While several authors have reported successful modulation of channel conduction in Li-based EIS with write pulse lengths as short as 5 ns,^[46] 100 ns,^[60] and 1–10 ms,^[35,38] generally an additional delay time of at least 50–100 ms is needed before reading the conductance level so that the conductance has time to stabilize. Bishop et al. were the first to collect detailed, time-resolved EIS conductance data with sub-microsecond resolution following 100 ns write pulses.^[60] For a LiPON/WO₃ device with 100 μm channel length, they found that after a 100 ns write pulse, there continues to be channel conductance change over millisecond timescales. By fitting a distributed equivalent circuit model to the time-resolved data, Bishop et al. extracted two effective time constants: τ_{vert} for charge transfer through

the electrolyte to the electrolyte/channel interface capacitor and τ_{horz} for charge redistribution in the channel. τ_{vert} depends only on the transport properties of the electrolyte, while τ_{horz} depends on the channel length and conductance. For the measured device, with 100 μm length channel, $t_{\text{read}} = 96$ ms and is dominated by $\tau_{\text{horz}} = 350$ μs while τ_{vert} is much smaller, 35 μs. Based on scaling arguments from their model, Bishop et al. argued that as channel lengths are reduced, τ_{horz} will also be reduced until τ_{vert} is the limiting timescale. Bishop et al. projected that for a scaled device with 100 nm length channel and 10× decrease in electrolyte resistivity, τ_{horz} will be greatly lowered to ≈3.5 ns, while $t_{\text{read}} = \tau_{\text{vert}} = 3.5$ μs.

The small size of Li⁺ has resulted in Li-based EIS devices with excellent endurance over many cycles. The knowledge of many intercalation materials for Li⁺ from the battery literature has allowed for choice of channel materials which operate in an appropriate resistance range. Furthermore, symmetric device geometries have allowed for low operating voltages. Optimization of the kinetics for Li⁺ ion transfer through the electrolyte and at the electrolyte/channel interface in EIS has yielded devices with linear and symmetric updates. Scaled devices have been shown to operate with write times as short as 5 ns. However, channel conductance transients after write pulses are much longer. Additionally, the most significant drawback of Li⁺ is its potential to contaminate silicon devices when integrated with CMOS circuitry.

4.2. Oxygen-Ion-Based

Oxygen-anion-based EISs are attractive for their good compatibility with CMOS processing and environmental stability. Like the Li-based devices, most materials for O-based EIS are compatible with conventional lithography techniques, are stable at elevated temperatures, and can be deposited by either radio frequency (RF) or direct current (DC) reactive sputtering. Unlike Li⁺, O²⁻ anions do not present a contamination risk to silicon devices.

Generally, the operation of oxygen-ion-based EIS involves the migration of oxygen ions or vacancies and redox reactions at the channel changing the oxygen stoichiometry in the channel materials. A wide range of oxides such as SmNiO₃, SrCoO_x, TiO_{2-x}, Pr_{0.7}Ca_{0.3}MnO_{3-x}, and WO₃ have been explored as the channel material. Ionic liquids^[63,64] and solid-state electrolytes^[36,65,61] have been used as electrolyte. Y₂O₃-stabilized ZrO₂ is a very commonly used electrolyte material, which shows good ionic conductivity at elevated temperatures and has been widely studied and applied in solid-state fuel cells.^[66]

Li et al. reported a relatively fast modulation speed for O²⁻-based devices, with 2 μs write pulses, but at an elevated temperature of 170 °C.^[65] Li et al.'s devices were based on TiO_{2-x} channel material and YSZ electrolyte. They investigated the relationship between write time, electrolyte thickness, and operating temperature and fit their data to the simple relationship

$$\tau_w = DL\rho(T) \quad (3)$$

where D is a fit parameter, L is the thickness of the YSZ electrolyte, and $\rho(T)$ is the temperature-dependent ionic resistivity

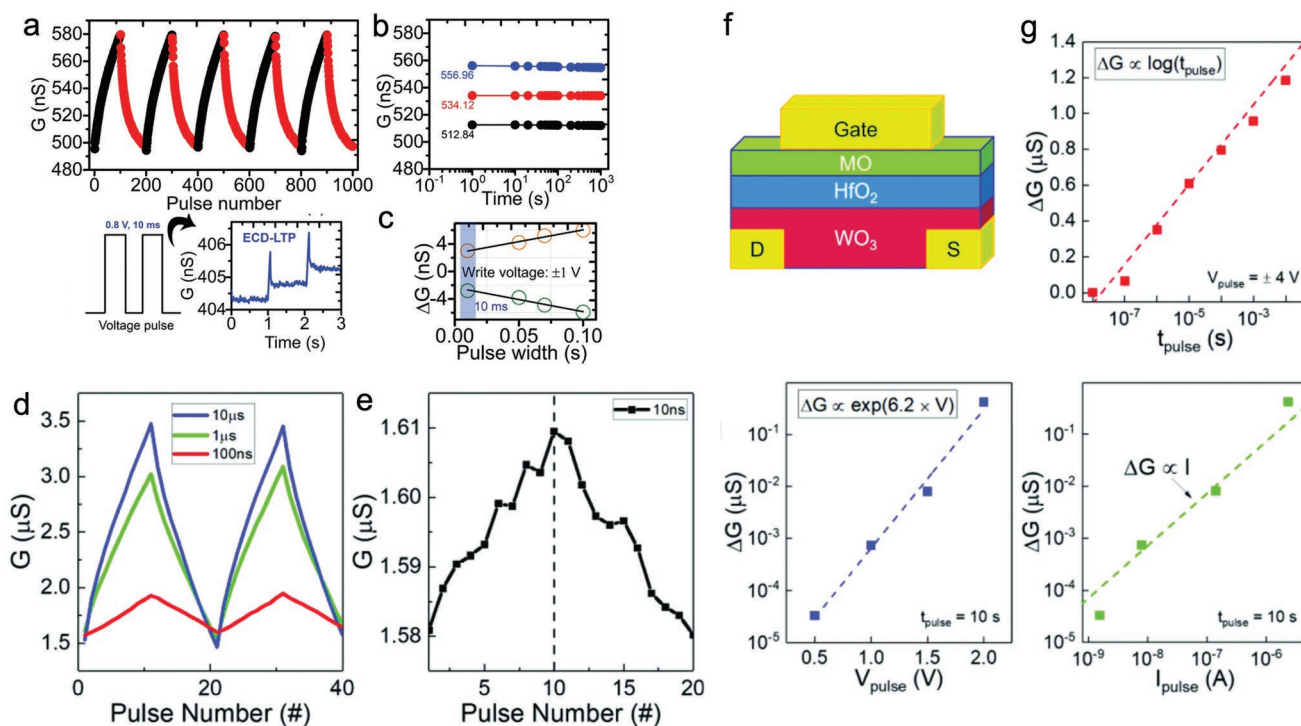


Figure 3. Summary of progress in O-based devices. a–c) Endurance of YSZ/WO₃ EIS device developed by Nikam et al. over 10³ voltage pulses (± 1 V, 10 ms pulses with 1 s delay). This device also shows good state retention (b) and linear scaling of ΔG with pulse width down to 10 ms (c). Adapted with permission.^[61] Copyright 2021, Wiley-VCH. d–g) Characteristics of state-of-the-art HfO₂/WO₃ device developed by Kim et al., including potentiation/depotentiation behavior during ± 4 V (d) 100 ns–10 μ s pulses and (e) 10 ns pulses, (f) device schematic, and (g) scaling relationships of ΔG . Unlike Nikam et al., Kim et al. found that ΔG scales with the log of pulse width. Adapted with permission.^[62] Copyright 2019, IEEE.

of the electrolyte. Ionic transport through the electrolyte is the rate-limiting step in these devices since the YSZ is over 800× thicker than the TiO_{2-x} layers. Based on these results, the write pulse length could be further decreased by increasing temperature or decreasing the thickness of the electrolyte.

Similar to what has been observed for Li-EIS, the linearity of the channel conductance as a function of pulse number in O-EIS has been related to the ionic conductivity of the electrolyte. Nikam et al. showed that devices using a YSZ electrolyte deposited in an oxygen-free environment show linear and nonvolatile conductance updates (Figure 3a–c) as compared to devices using YSZ deposited under high oxygen flow rates. They attributed the poor performance of the YSZ electrolyte deposited under high oxygen flow rates to the low concentration of oxygen vacancies in this film, leading to low O²⁻ conductivity. We question this argument, as explained below. The device shows nonvolatile modulation in its channel conductance for a sequence of just a few pulses due to the presence of oxygen vacancies near the YSZ/WO₃ interface. Further pulsing leads to the accumulation of oxygen ions at the interface due to the inability of O²⁻ to migrate through the bulk of YSZ. This creates nonlinear and volatile changes in the conductance of the channel. However, while Nikam et al. claimed to validate their claim that changing the flow rate of oxygen during YSZ deposition changes the concentration of oxygen vacancies, we question whether changing the flow rate alone can significantly alter the YSZ's oxygen vacancy content. Oxygen vacancy concentration in YSZ is fixed by the concentration of Y dopants,

across a very wide range of oxygen chemical potentials. Reducing YSZ requires strongly reducing conditions (e.g., H₂ gas at elevated temperatures), and the reduction of Zr⁴⁺ introduces electronic conductivity into the material. We do not think the conditions in Nikam et al. placed YSZ into that regime. It is possible instead that the authors modified the microstructure of their YSZ films,^[67] causing changes in the effective ionic conductivity.

The only report of an O-EIS device that operates with short enough write pulses for practical applications comes from Kim et al.^[62] They developed a device with WO₃ active layer and metal-oxide (MO) ion reservoir, separated by a HfO₂ electrolyte. A schematic is shown in Figure 3f. With voltage pulses of ± 4 V, Kim et al. demonstrated fairly linear and symmetric conductance modulation for pulse widths between 10 μ s and 100 ns (Figure 3d). Shown in Figure 3e, Kim et al. also demonstrated conductance modulation with pulse widths as short as 10 ns. However, with these short pulses, the conductance updates are very nonlinear and asymmetric, and the devices have a small on/off ratio, ≈1.02. Furthermore, Kim et al. noted that due to circuit parasitics, the actual pulse width applied to the device may be longer, and channel conductance transients in O-based devices still need to be investigated.

Kim et al. additionally make interesting observations about the scaling of ΔG with pulse width, t_{pulse} , current, I_{g} , and voltage, V_{g} , shown in Figure 3g.^[62] As expected, they found that with constant voltage gating, ΔG scales linearly with I_{g} . However, Kim et al. found that ΔG is logarithmically dependent on

t_{pulse} . This is in contrast to Li-based EIS where ΔG scales linearly with both t_{pulse} and I_g .^[46] It is also contrary to the findings of Nikam et al.^[61] that ΔG also scales linearly with t_{pulse} in O-based devices. This discrepancy could be due to the slow movement of O^{2-} ions compared to Li^+ ions, such that the change in O^{2-} ion concentration per pulse is more weakly dependent on write time. Furthermore, Kim et al. found that ΔG is exponentially dependent on V_g . Kwak et al. also observed an exponential dependence of ΔG on operating voltage, with a saturation of ΔG for $V_g \gtrsim 2.5$ V. A more detailed explanation for these relationships and the discrepancy between Kim et al. and Nikam et al.'s results should be investigated by future studies.

While Kim et al.'s work demonstrated that O-based devices can operate with the same speed as devices based on smaller ions, the size of the O^{2-} ion still presents concerns relating to the operating voltage, energy consumption, and small channel conductance change.^[68] Most reported O-EIS devices operate at higher voltages, $V_g = 3\text{--}4$ V. Kwak et al. investigated the relationship between on/off ratio and operating voltage in their devices which consist of GdO_x ion reservoir, HfO_x electrolyte, and WO_3 channel. They found that on/off ratio increases with increasing operating voltage and reaches over 5000 at $V_g = 3$ V. However, to achieve an on/off ratio of 10, a voltage of at least ≈ 2.0 V is needed. In terms of energy, while many reports of O-EIS do not include a calculation of write energy, Kim et al. projected that once O-EIS has been scaled to 100×100 nm², the energy consumption per ΔG will be equivalent to Li-EIS at 100 fJ nS⁻¹. It is unclear whether this energy calculation accounts for the electrostatic CV^2 contribution.

While O^{2-} offers advantages to Li^+ in terms of CMOS compatibility and could match Li^+ in terms of energy consumption once devices are scaled down, the larger size of the oxygen ion presents new challenges for EIS devices compared to the Li ion. Individual reports have separately demonstrated 1 V operating voltage, 100 ns write lengths, and good on/off ratios. However, no single device has all of these features combined. In order to

achieve all of these requirements at once, O^{2-} transport kinetics in devices at room temperature must be improved, which remains the greatest challenge for O-EIS.

4.3. Organic, Proton-Based

Organic electrochemical transistors (OECTs), first developed in the mid-1980s, function by ion injection from an electrolyte to modulate the conductivity of an organic semiconductor channel, and can be thought of as an amplifier, similar to metal-oxide-semiconductor field-effect transistors (MOSFETs) and organic field-effect transistors (OFETs).^[69] Organic EIS differ from OECTs in that in EIS the electrolyte separates the channel from an ion reservoir layer, and after programming, the electrodes are disconnected so that there is no source of compensating charge for ions to move back across the electrolyte, making programmed conductance states nonvolatile. Nevertheless, semiconducting polymers which have been developed for OECTs can be implemented in organic EIS devices. One example is PEDOT:PSS, the chemical structure of which is shown in Figure 4a. PEDOT is a p-type semiconducting polymer in which mobile holes carry current hopping from one chain to another. The sulfonate anions in PSS compensate for these holes. Upon application of a positive gate bias, cations are injected from the electrolyte into the channel, compensating the sulfonate anions and decreasing the number of holes and the channel conductance.^[69]

The first report of an organic EIS device based on protonation of the channel material comes from van de Burgt et al.^[70] They refer to their device as an electrochemical neuromorphic device. It consists of a PEDOT:PSS gate, Nafion solid electrolyte, and PEDOT:PSS film partially reduced with poly(ethylenimine) (PEI) as the channel. PEI stabilizes the neutral form of PEDOT, allowing the channel to maintain its oxidation state. Van de Burgt et al. achieved 500 conductance states with ± 1 mV

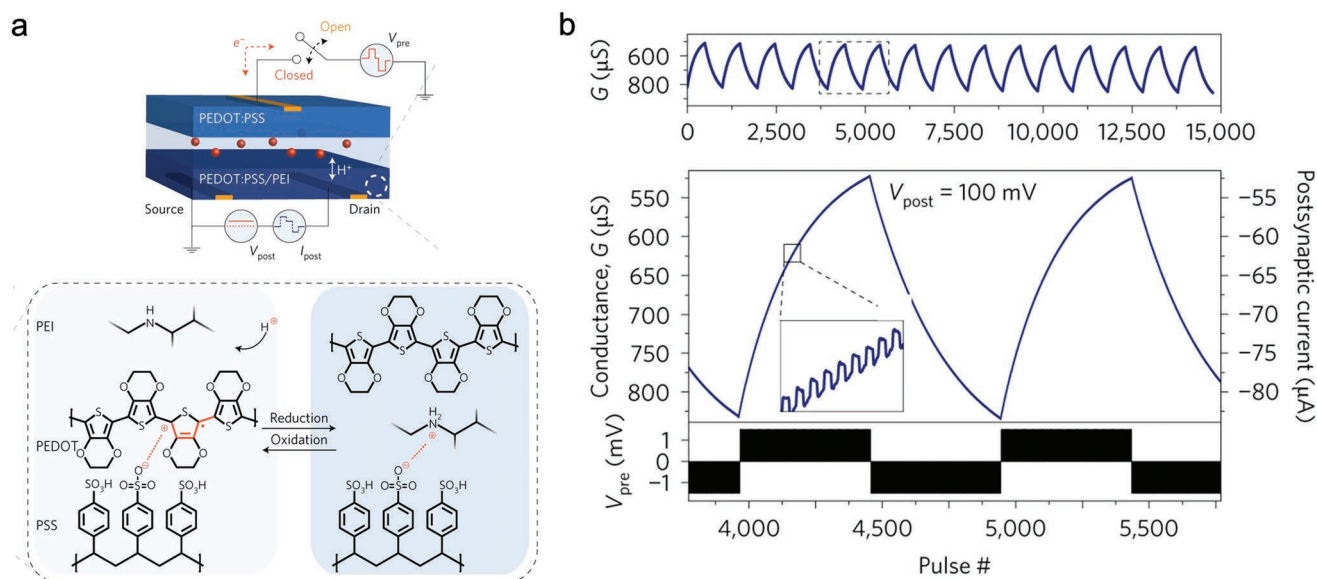


Figure 4. a) Schematic of device reported by van de Burgt et al. and chemical structure of channel materials PEDOT:PSS and PEI. b) Potentiation/depotentiation behavior of device. Adapted with permission.^[70] Copyright 2017, Macmillan.

operating voltage (Figure 4b). However, ΔG achieved between the minimum and maximum resistance states is small, barely twofold, and the device is not particularly fast; write times of at least 6 ms are required for nonvolatile conductance modulation. This is consistent with the estimated timescale for proton diffusion in the channel $\tau \approx 10$ ms based on the charge carrier diffusivity of PEDOT:PSS, $\approx 10^{-8}$ cm² s⁻¹. Van de Burgt et al. confirmed that energy consumption scales with device area. They projected an ionic transfer energy cost of 35 aJ per write pulse for a $0.3 \times 0.3 \mu\text{m}^2$ device area. Despite concerns that the high mobility of protons may create issues for long-term retention of states, van de Burgt et al. found that there is only a 0.04% standard deviation in conductance for devices measured over 25 h.

Parallel arrays based on organic EIS have also been demonstrated. Fuller et al. combined a volatile conductive bridge memory (CBM) with an organic EIS using the same PEDOT:PSS/Nafion material system reported by van de Burgt et al.^[71] The CBM has highly nonlinear *IV* characteristics and serves as a selector that connects to the gate terminal of the EIS device. When operating in an array, if the voltage drop on a cross point is higher than the threshold of the CBM device, the EIS will be updated, however the nontargeted devices have lower voltage than the threshold, and the CBM blocks gate current of the EIS retaining its state. As a result, the combination arranged in a crossbar array allows highly selective and parallel addressing. The method should be applicable to other types of devices discussed in this review. The good linearity, near perfect symmetry, and low write variance of the organic EIS are expected to achieve similar ANN accuracy with an ideal array. Furthermore, Fuller et al. reported devices being programmable with write pulses as short as 200 ns, followed by a 500 ns read time. They attributed this fast operation to the high mobility of protons in PEDOT:PSS.

One major advantage of organic EIS is that the charge carrier mobilities of organic materials are generally much lower than crystalline semiconductors, making low-conductance states easier to achieve in organic channel materials. Furthermore, the off-state conductivity of semiconducting polymers can be tuned by molecular design, processing, and blending.^[72] For example, Fuller et al. adjusted the ratio of PEDOT to PSS in their channel material to 1:14 in order to lower the average channel conductance to <100 nS.^[71] Furthermore, chemical additives or synthetic backbone design of organic semiconductors could be used to shift the DOS to optimize the linearity of dG versus dQ .^[72]

Another major advantage of organic EIS is the speed. In one of the most impressive reports of an organic EIS to date, Melianas et al. achieved linear and symmetric conductance modulation with write pulses as short as 20 ns, with sub-microsecond total write plus read time.^[73] Melianas et al.'s device used a previously reported ion gel electrolyte consisting of polymeric insulator poly(vinylidene fluoride-*co*-hexafluoropropylene) (PVDF-HFP) mixed with ionic liquid 1-ethyl-3-methylimidazolium bis(trifluoromethylsulfonyl)imide (EMIM:TFSI). They replaced PEDOT:PSS as the channel and reservoir materials with recently developed semiconducting polymer poly(2-(3,3-bis(2-(2-(2-methoxyethoxy)ethoxy)ethoxy)-[2,2-bithiophen]-5-yl)thieno[3,2-*b*]thiophene) (p(g2T-TT)). Compared to PEDOT:PSS, p(g2T-TT) is very resistive prior to ion insertion (microsiemens

compared to millisiemens off conductance) and enables a larger dynamic range (4 \times compared to $\approx 1.3\times$) for even shorter write pulses (300 ns compared to 1 μs) of ± 1 V. The p(g2T-TT) also has very low energy consumption, ≈ 80 fJ for a $45 \times 15 \mu\text{m}$ channel area. Melianas et al. projected that for a $1 \times 1 \mu\text{m}$ area device, the energy per write would be <1 fJ.

Packaged semiconductor devices regularly reach temperatures up to 90 °C during operation, and the temperature stability and dependence of device characteristics has largely been unexplored for most EIS devices. Melianas et al. found that the cycling characteristics of their device using p(g2T-TT) are largely temperature-independent up to 90 °C, with only a 3% increase in mean channel conductance and 4% increase in dynamic range due to increased injected charge per pulse at elevated temperature.^[73] They suggested that choosing an electrolyte with ionic conductivity which is more weakly dependent on the temperature could further reduce the temperature dependence of device characteristics. Furthermore, the p(g2T-TT) device can endure many cycles at this elevated temperature. After 1×10^9 write-read events, they observed 2.4% decrease in the median channel conductance; after 2×10^9 write-read events, there is a 12.8% change in conductance.

Despite the advantages of organic materials for EIS, there are also many concerns. One concern is the operational environment that is required for these devices. The conductivity of many proton conductors deteriorates rapidly in the absence of moisture. This is problematic as standard electronics packaging procedures create dry conditions. Furthermore, many organic semiconductors like PEDOT:PSS are susceptible to oxidation in the presence of environmental oxygen.^[72] However, these challenges are not insurmountable. Melianas et al. showed that unlike PEDOT:PSS devices, their p(g2T-TT) devices can operate in dry conditions (under vacuum).^[73] Additionally, Keene et al. investigated the mechanisms for instability in PEDOT/PEI:PSS devices and methods for mitigating them.^[74] They proposed that at reducing potentials (+V), O₂ gas from the environment diffuses into the channel and reacts with electrons from PEDOT and protons from PEI to form water. The loss of electrons from PEDOT leads to a rapid decrease in channel conductance. This degradation mechanism can be prevented by operating in an inert environment. At oxidizing potentials (-V), PEDOT is reduced by the strongly reducing amines on PEI, decreasing channel conductance. The rate of this reaction is increased with increasing PEI concentration. However, increasing PEI concentration also helps to stabilize PEDOT under reducing potentials. Thus, Keene et al. found that there is an optimum PEI concentration of 50 mol%. Furthermore, instability during cycling is caused by the diffusion of neutral PEI molecules out of the channel. This can be mitigated by the use of a solid-state electrolyte like Nafion instead of a liquid electrolyte. Based on these findings, Keene et al. reported an encapsulation method done in an inert atmosphere to improve the device state retention time from <1 to ≈ 10 min.

Another concern is the scalability of organic EIS, given that these materials are generally not compatible with BEOL CMOS processing, both in terms of withstanding temperatures up to ≈ 400 °C and being patternable by common lithographic techniques. Most reported organic EIS devices have channel lengths that are at least 10 μm long, and PEDOT:PSS decomposes around

300 °C. Tuchman et al. have developed a way around the lithography barrier by developing a stacked hybrid organic/inorganic EIS (SHOE).^[75] A SHOE consists of two organic semiconductor films (channel and gate) separated by a porous inorganic electrolyte which is permeated by an ionic liquid. The device is fabricated by first spin-coating a PEDOT:PSS film on an insulating substrate patterned with Au contacts. A thin SiO₂ film is then deposited on top by high-density plasma chemical vapor deposition (HDPCVD) and saturated with 1-ethylimidazolium bis(trifluoromethylsulfonyl)imide. The gate PEDOT:PSS film is then spin-coated on top. A gold layer is evaporated over the entire device to protect the PEDOT:PSS during lithography and etching and to serve as the gate contact. After the lithography and etch steps are complete, the device is encapsulated with an atomic layer deposition Al₂O₃ layer to protect against ambient moisture and serve as an ionic liquid diffusion barrier and another HDPCVD oxide layer to serve as a low-*K* dielectric between the metal layers. This process allows for the fabrication of devices with channel lengths down to 1 μm and is limited by the lithographic exposure resolution. Tuchman et al. found that their scaled-down devices exhibit superior device characteristics compared to previously reported devices with PEDOT:PSS. The dynamic range of devices is shown to increase linearly as the device area is decreased. Scaled devices show a 2× dynamic range across 100 conductance states and can be operated with sub-microsecond total write–read time (100 ns write + 200 ns delay + 500 ns read). However, compatibility with CMOS processing remains one of the biggest challenges for organic EIS.

In addition to the impressive performance and well-developed parallel addressing scheme, organic EIS may also provide unique opportunities for biointerfacing because the materials can be easily fabricated on flexible plastic substrates and have good biocompatibility. This application would not have the same stringent scaling and fabrication requirements as demanded for computation.

Organic EIS based on the movement of protons offers many advantages due to the small size of H⁺. Write pulses as short as 20 ns have been demonstrated, with total write + delay + read times being around 1 μs, much faster than Li- and O-based devices but perhaps still too long to meet the requirements discussed in Section 3. While many organic materials suffer from stability issues or rely on environmental moisture for proton conduction, these issues can be overcome. The versatility of organic channel materials allows for the development of novel semiconducting polymers like p(g2T-TT), which have ideal properties for EIS, including fast kinetics, linear dependence of d*G* on d*Q*, and temperature-independent properties up to 90 °C. However, the dynamic range of organic channels, including p(g2T-TT), is generally too small. Furthermore, compatibility with BEOL processing, in particular the higher temperatures which must be endured, remains a major challenge for organic EIS. This has motivated the search for inorganic devices which operate by the movement of protons.

4.4. Inorganic, Proton-Based Devices

The promising performance of organic EIS based on proton intercalation has motivated creating H⁺-based devices with

inorganic materials which are scalable and compatible with CMOS processing. In the first of these, Yao et al. demonstrated an EIS device which shuffles protons between a solid hydrogen reservoir PdH_x and the channel-active material WO₃, using a Nafion electrolyte (Figure 5a,b).^[39] The use of a solid hydrogen source, a metal hydride, rather than liquid water, has been the enabler of this first solid state, inorganic proton-based device. They showed an extremely large continuum range of resistance states, over seven orders of magnitude, arising from increasing the H content from nominally 0 in WO₃ (W⁶⁺) to 1 in HWO₃ (W⁵⁺), as shown in Figure 5c. Furthermore, they investigated the mechanism for conductivity change of WO₃ across different regimes, and found that hydrogen serves as n-type donor creating large polarons when H concentration is less than 10%, and the material becomes metallic and undergoes phase change above 10%. They found that the low conductance regime offers better symmetry and greater dynamic range (Figure 5d), while the high conductance regime offers greater change in conductivity per pulse. Additionally, Yao et al. calculated an ionic transfer energy consumption of 18 aJ (μm² × nS)⁻¹, if the devices could be scaled down to the μm² regime, and demonstrated device endurance of >20,000 pulses. Even with constant current gating, Yao et al. observed a small degree of asymmetry in their device. Furthermore, Yao et al. reported that the asymmetry ratio varies depending on the channel conductance range in which pulsing is done. In high conductance regime, the asymmetry ratio is 0.36, while in low conductance regime, the symmetry is much improved to a ratio of 0.17.

While Yao et al.'s work was very encouraging for low energy and controllable modulation of inorganic, proton-based EIS devices, the use of Nafion polymer as a solid-state electrolyte is not compatible with nanofabrication using CMOS-compatible processes. A few other works have investigated proton devices that use inorganic electrolytes based on silicon dioxide. Lee et al. reported a transistor-like device with WO_x channel and SiO₂-H electrolyte, and no separate reservoir.^[76] They optimized the state-update behaviors of the device by modifying the proton concentration and thickness of the electrolyte. However, without a well-defined *n* ion reservoir, this device is likely working by relying on water uptake into the electrolyte in ambient, making its repeatable controllability a challenge.

Onen et al. replaced the Nafion electrolyte in Yao et al.'s device with nanoporous phosphosilicate glass (P-SiO₂, PSG) as the electrolyte (Figure 6a,b).^[77] PSG has a proton conductivity up to 2.54 × 10⁻⁴ S cm⁻¹ at room temperature, is a good electronic insulator, and is readily available in conventional Si processing. In PSG, the presence of phosphorus increases the number of nonbridging oxygen bonds, the pore volume, and the surface area, giving PSG its high proton conductivity. Onen et al. deposited the PSG layer using plasma-enhanced chemical vapor deposition, and patterned various gate lengths between 2 and 100 μm. Operating with 1 s, ± 3 V pulses, in Figure 6c, they showed very linear and symmetric conductance modulation with little variation in conductance values over 50,000 pulses (Figure 6e). Furthermore, Onen et al. reported that the energy consumption of a device with 200 μm² area is just 0.45 mJ S⁻¹, 1000× more energy efficient than the O-based device of the same area reported by Kim et al.^[62]

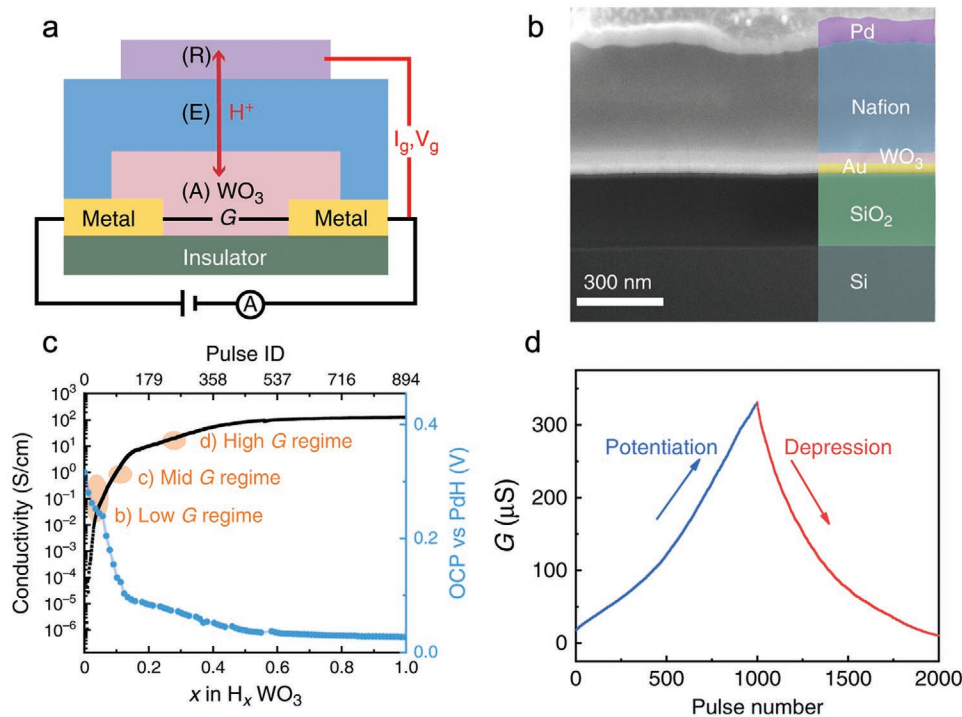


Figure 5. a) Schematic of proton-based device using inorganic channel developed by Yao et al. b) Scanning electron microscopy image of device cross-section. c) Electronic conductivity of H_xWO_3 in the EIS device, and open-circuit potential (OCP) of the device (channel WO_3 vs gate PdH_x) as a function of hydrogen content in the channel. d) Average conductance value of channel after application of ± 200 nA, 5 ms pulses. Adapted under the terms of the CC-BY Creative Commons Attribution 4.0 International license (<https://creativecommons.org/licenses/by/4.0>).^[39] Copyright 2020, The Authors, published by Springer Nature.

In later work, Onen et al. demonstrated modulation of PSG EIS with pulses as short as 5 ns using an operating voltage of 10/−8.5 V.^[26] Besides high modulation speed, these EISs show nearly linear and symmetric behavior, state retention over $10^{10} \times$ the pulse time, good endurance, and an optimal base resistance of 88 M Ω , as shown in **Figure 7**. The energy consumption of proton transfer in the EIS while the pulse voltage is at its peak value is estimated to be 15 aJ per pulse. PSG has a critical field (8–15 MV cm^{−1}) which is much higher than the breakdown field or electrochemical stability window of most electrolyte materials. This allows for application of electric fields so large, that the activation barrier for proton hopping (≈ 0.4 eV) might be completely removed, enabling proton transport at extreme speeds across PSG. At longer pulse lengths, Onen et al. speculated that the low diffusivity of protons in H_xWO_3 leads to buildup of protons at the channel/electrolyte interface, limiting further insertion of protons and potentially leading to H_2 gas evolution. Indeed, catastrophic failure of devices consistent with bubble formation due to H_2 gas evolution is observed when the pulse length is increased to 90 ns.

Nikam et al. provided another example of an inorganic proton-based device using WO_3 as the channel material and Si–H as the proton reservoir.^[78] For the electrolyte, they used a single layer (0.33 nm thick) hexagonal boron nitride (hBN), which is electronically insulating and has proton permeable pores in the centers of its hexagonal rings. Nikam et al. found that while there is a small amount of electronic current leakage through the hBN (≈ 8 pA), it is much improved compared to using no electrolyte, the Si–H alone, which has a leakage of

13 nA at 0.5 V. While the transfer of large-scale 2D materials can pose a challenge to the integration of these materials, Nikam et al. fabricated wafer-scale devices by rolling CVD grown hBN-thermal tape onto the WO_3 channel pattern and using a subsequent heat treatment to release the tape. The devices show excellent symmetry and linearity ($\alpha = 0.9/0.9$), good endurance and retention (<5% change in G_{max} over 10^4 pulses), and are operated with ± 1 V, 10 ms pulses.

The achievements of the inorganic proton-based devices are very promising. Beyond solving the issues with CMOS compatibility of organic devices, they have shown fast modulation with 5 ns pulses, high energy efficiency (down to 15 aJ per state), good symmetry and linearity, and excellent dynamic range over seven orders of magnitude. However, low voltage (≈ 1 V) nanosecond modulation of inorganic proton devices is yet to be addressed.

4.5. 2D-Material-Based

We have already discussed examples of 2D materials such as hBN and graphene being used as electrolytes or ionic sieves in EIS devices based on protons^[78] and Li ions,^[35] respectively. 2D materials such as graphene (**Figure 8c–e**)^[79] and titanium carbide MXene ($Ti_3C_2T_x$) (**Figure 8a,b**)^[80] have also attracted interest as channel materials. 2D materials are very attractive for their ability to decrease the postpulse relaxation in the channel, potentially yielding very high-speed modulation.

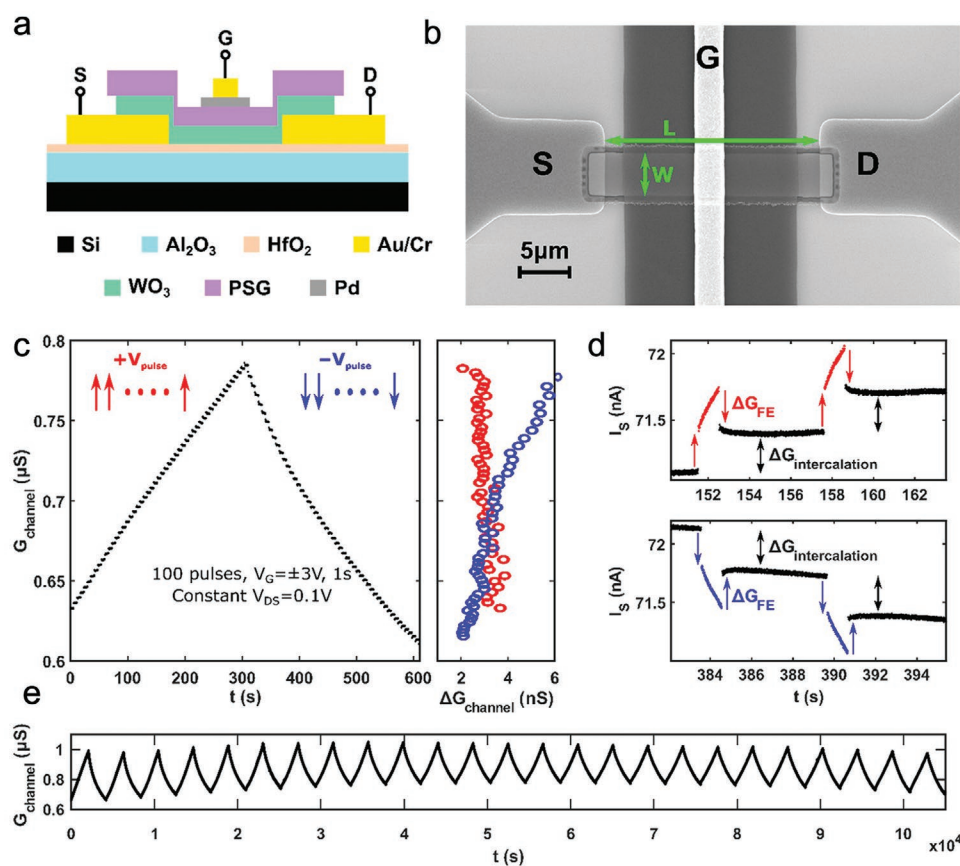


Figure 6. a) Schematic of all inorganic device based on proton intercalation reported by Onen et al. b) Scanning electron microscope image of device source (S), drain (D), and gate (G) with channel width (W) of 5 μm and a length (L) of 25 μm . c) Potentiation/depotential behavior of device over 100 pulses of $\pm 3\text{ V}$, 1 s. d) Detailed view of (c) where the source–drain current is constantly recorded during the gate pulse (colored) and between gate pulses (black). e) Endurance characterization of device over 50 000 pulses. Adapted with permission.^[77] Copyright 2021, American Chemical Society.

Melianas et al. reported an EIS device based on proton intercalation into 2D titanium carbide ($\text{Ti}_3\text{C}_2\text{T}_x$) MXene (Figure 8a).^[80] MXenes are a family of 2D materials with the general formula $\text{M}_{n+1}\text{X}_n\text{T}_x$, where M is a transition metal, X is carbon and/or nitrogen, n is between 1 and 4, and T_x represents mixed surface terminations ($-\text{O}$, $-\text{F}$, $-\text{Cl}$, and $-\text{OH}$). Ions, organic molecules, and polymers can intercalate between the layers of MXenes; furthermore, the electronic and electrochemical properties of MXenes can be tuned by varying compositions and structures, as well as the chemistry of their surfaces and interlayers.^[81] Melianas et al. explained that the titanium atoms in the titanium-carbide core layers of $\text{Ti}_3\text{C}_2\text{T}_x$ give it its high electronic conductivity, while fast and reversible surface redox reactions are enabled by surface-functional groups, which give it a metal–oxide-like surface.^[80] Additionally, multilayer $\text{Ti}_3\text{C}_2\text{T}_x$ films can perform at extreme charging rates as high as 1000 V s^{-1} . It is also stable for several years in ambient conditions and at temperatures up to $830\text{ }^\circ\text{C}$. For their device, Melianas et al. used $\text{Ti}_3\text{C}_2\text{T}_x$ assembled by a layer-by-layer (LbL) technique, as both the ion reservoir and channel, with PVA– H_2SO_4 as the electrolyte. The LbL techniques allow the insertion of positively charged spacer molecules between the negatively charged $\text{Ti}_3\text{C}_2\text{T}_x$ flakes, changing the $\text{Ti}_3\text{C}_2\text{T}_x$ films from metallic to semiconducting. To demonstrate the

tunability of $\text{Ti}_3\text{C}_2\text{T}_x$, Melianas et al. investigated three different spacer molecules: tris(3-aminopropyl)amine (TAPA), tris(2-aminoethyl)amine, and PEI. They found that during a high rate (8 V s^{-1}) gate voltage sweep, $\text{Ti}_3\text{C}_2\text{T}_x/\text{TAPA}$ showed almost no hysteresis and good dynamic range, while the other spacers showed more pronounced hysteresis. Devices with channels consisting of six bilayers of $\text{Ti}_3\text{C}_2\text{T}_x/\text{TAPA}$ can be tuned over 50 states with 200 ns pulses and a read–write delay of only 1 μs , as shown in Figure 8b. This is similar in speed to state-of-the-art proton-based organic devices and faster than any metal–oxide-based device. Moreover, the ionic transfer energy consumption per write operation is only $80\text{ fJ } \mu\text{m}^{-1}$, and the device showed good endurance over 10^8 write–read events. The major weakness of these devices is that they operate in millisiemens conductance range and show significant device-to-device variability.

The major advantage of 2D materials as the channel material is the speed with which ions can redistribute in the channel following write pulses. The devices we have discussed implement few-layer 2D materials as the channel, but monolayer channels should provide the ultimate speed by eliminating the ion redistribution through the depth of the channel. While the fastest write pulse shown with few-layer 2D materials is currently 200 ns with a read–write delay of 1 μs , which does not meet the requirement outlined in Section 3, it is much faster than

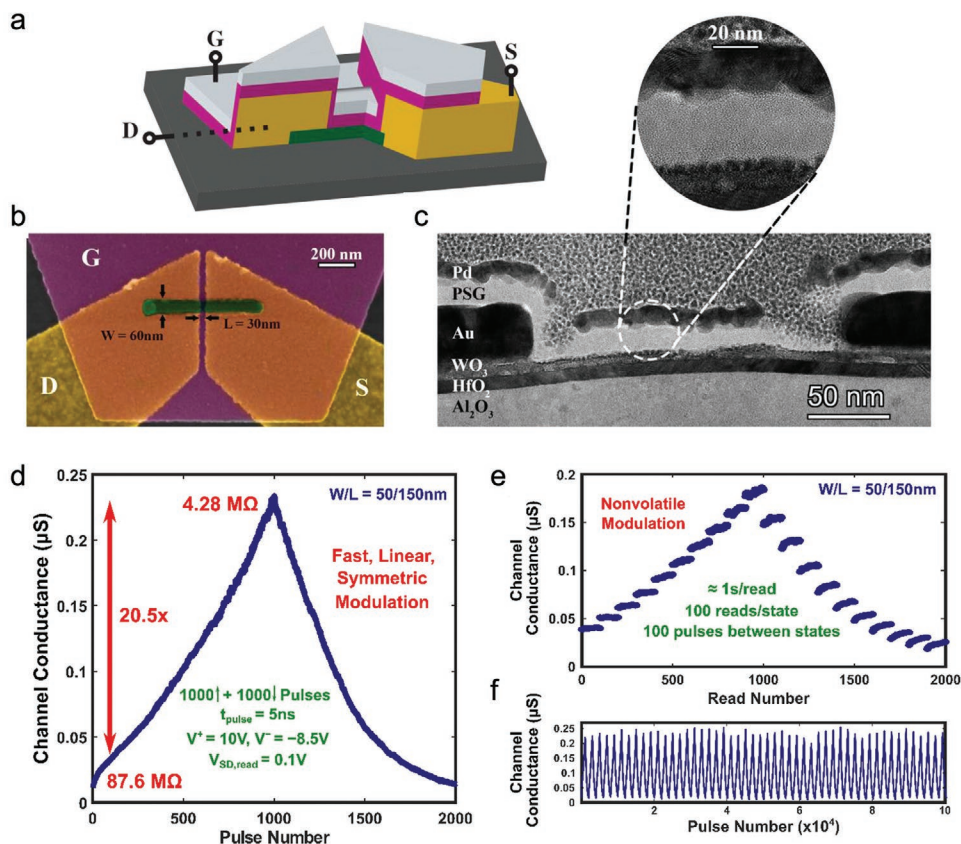


Figure 7. a) Schematic of nanosecond programmable EIS devices reported by Onen et al. showing Au (yellow), WO_3 (green), PSG (magenta), and Pd (gray) layers. b) False-colored scanning electron microscopy image of a device. c) Transmission electron microscopy image of device cross-section after extensive modulation. d) Channel conductance of 50 nm \times 150 nm device during modulation by 5 ns pulses. e) Retention of channel conductance over ≈ 100 s at different conductance levels. f) Device endurance over 10^5 pulses. Adapted with permission.^[26] Copyright 2022, The Authors, published by American Association for the Advancement of Science.

any 3D inorganic channel material. EIS based on 2D materials has also met the requirements for operating voltage (1 V) and dynamic range ($\approx 10\times$), and has good endurance. Retention of conductance states may need to be improved for some 2D channels by optimization of device geometry and encapsulation. The most significant limitation of 2D materials is that all reports of EIS using 2D channels combine them with polymer electrolytes which are not compatible with CMOS processing. Future research should investigate integrating 2D channels with inorganic electrolytes.

4.6. Remaining Challenges

As discussed above, electrochemical ionic synapses have shown fast programming pulses, low energy consumptions, good repeatability, and low variance, as summarized in Table 1. However, the devices reported so far have not fully met the desirable specifications simultaneously in a given device, as outlined in Section 3. Based on Table 1, it is clear that while many devices can operate with voltages around 1 V, the voltage that is required to achieve nanosecond operation is still above 1 V.^[46,62,82] Operation under ≈ 1 V is needed for improved energy efficiency and for compatibility with standard integrated circuit

drivers. In addition, many devices have a dynamic response long after the programming pulses before reaching a stable conductance state, requiring a delay time between write and read events.^[60] So far, this delay time is hundreds of nanoseconds to 1 μs for organic and 2D channels and 50–100 ms for 3D inorganic channels. Furthermore, there is often a trade-off between operating voltage, pulse length, and dynamic range. While the requirements for each of these parameters alone (≈ 1 V operating voltage, ≈ 10 ns pulses, $\approx 10\times$ dynamic range) has been met in various devices, meeting all three requirements with a single device remains a major challenge. As discussed in Section 3, it is desirable to have energy-efficient devices that operate at 1 V with nanosecond pulses and fast settling. In order to achieve these goals, a physical model of the devices that bridges the dynamic processes with material properties can potentially provide insights and guidance for further research and development.

5. Physical Model of Electrochemical Ionic Synapses to Guide Material Design

In order to identify the required material properties to achieve the desired specifications described in Section 3, we construct

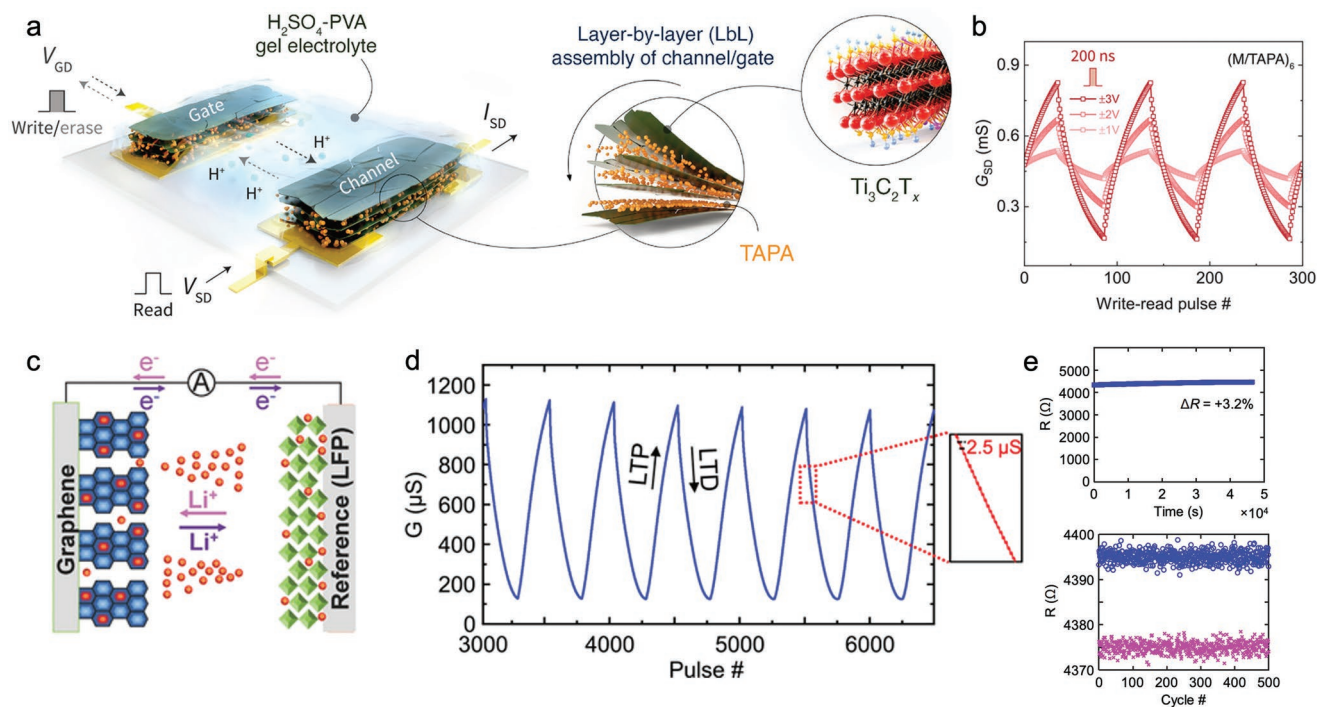


Figure 8. Summary of progress in devices based on 2D channels. a) Schematic of EIS device with MXene channel reported by Melianas and co-workers. b) Device potentiation/depotentiation behavior with 200 ns pulses of different constant voltage amplitudes. Adapted with permission.^[80] Copyright 2021, The Authors, published by Wiley-VCH. c) Schematic of EIS device with few-layer graphene channel reported by Sharbati et al. d) Device potentiation/depotentiation behavior over 250 distinct states with applied 10 ms constant current pulses of 50 pA. e) Demonstrated device retention over 13 h and endurance over 500 cycles. Adapted with permission.^[79] Copyright 2018, Wiley-VCH.

a physical model of the EIS. By simulations using this model, we deduce the ion conductivities and interface charge transfer kinetics needed to achieve the desired specifications, such as nanosecond modulation of conductance states while using 1 V or less gate bias. In addition, the model provides insights into the working mechanisms and dynamics from various voltage/current waveforms.

5.1. Model Description

The EIS device model is a 1D equivalent circuit model that considers ion transport through the electrolyte, charge-transfer reactions at electrolyte–gate and electrolyte–channel interfaces, and ion redistribution in the reservoir and channel layers. The model adapts standard elements in equivalent circuit models that are widely used for analyzing electrochemical impedance spectroscopy measurements on batteries and fuel cells.^[90,91] Our EIS model uses well-established equations to quantify ion transport and charge transfer kinetics under electric fields, with model parameters that relate to ion conductivity and rate coefficients.

The 1D geometry assumes that all physical quantities and processes are uniform in the lateral dimensions of the device, so any lateral diffusion or lateral voltage differences are not considered. This assumption is applicable when the gate completely covers the channel and the electrolyte resistance is much higher than the channel resistance. Also, in this model, we assume that the source and drain are shorted together.

The 1D equivalent circuit model is shown in **Figure 9a**. The electrolyte is modeled by a variable resistor R_E with a capacitor C_E in parallel.^[91] C_E represents the bulk ionic capacitance of the electrolyte, and R_E represents the resistance to ionic transport through the electrolyte. The ionic conductivity in the electrolyte, σ_E is a function of the electric field through the electrolyte and is given by^[92,93]

$$\sigma_E = \sigma_0(T) \frac{2k_B T}{q l_x V_E / t_E} \sinh \left(\frac{q l_x V_E / t_E}{2k_B T} \right) \quad (4)$$

where $\sigma_0(T)$ is the temperature (T)-dependent ionic conductivity in the low electric field limit, q is the ion charge, V_E is the voltage drop across the electrolyte, t_E is the thickness of the electrolyte, l_x is the ion hopping distance, and k_B is the Boltzmann constant.

Each of the two electrode interfaces (channel–electrolyte and reservoir–electrolyte interfaces) are modeled by a variable resistor, R_{ci} and R_{ri} , and a parallel capacitor, C_{ci} and C_{ri} , respectively.

The current flowing through the variable interfacial resistors is the Faradaic current that arises from the electrochemical reaction current density. The proposed model assumes a single-step charge transfer process, described by the Butler–Volmer model^[94] for each interface x , where x = reservoir–electrolyte or channel–electrolyte interface

$$j_x = j_{x0} \left(e^{\frac{\alpha_x z F V_x}{RT}} - e^{\frac{-(1-\alpha_x) z F V_x}{RT}} \right) \quad (5)$$

Table 1. Reported electrochemical ionic synapse device properties available in the literature.

Materials	Dimensions	Operating voltage	Pulse width	Dynamic range and number of analog states	Symmetry ^{a)}	Linearity ^{a)}	Energy consumption ^{b)}	Endurance/retention	Reference
Li⁺-based devices									
Channel: WO ₃ Electrolyte: LiPON	L: 10-100 μm	+2/+1.5 V	100 ns readable after 96 ms	15–35 nS 100+ states	V gating: 0.4 I gating: 0	V gating: 3.4/–3.7 I gating: 0.9/0.7	–	5 s	[60]
Channel: Li _{1-x} CoO ₂ Electrolyte: LiPON	t _{ch} : 120 nm t _{el} : 400 nm L: 2 μm	± 75 mV	2 s	4.5–270 μS ΔC ² /σ ² = 80	0	–	Projected 10 aJ for L = 200 nm	Several weeks 40 cycles	[23]
Channel: WO _{2.7} Electrolyte: Li ₃ PO ₄	L × W: 5 × 5 μm t _{ch} : 50 nm t _{el} : 100 nm	Two-step pulse scheme +3, –2/–2.5, +1 V	1.5 s	500 nS–3.5 μS	0.2	(0.60/–0.58) 0.7/–0.6	–	420 pulses	[49]
Channel: Li _x TiO ₂ Electrolyte: LiClO ₄ /PEO	L: 8 μm t _{ch} : 30 nm	± 0.2–0.3 V	10 ms readable after 50–100 ms	45–75 μS	0.1	–	2 fJ (μm ² × nS) ^{–1}	7 h 10 ⁶ pulses	[38]
Channel: LiCoO ₂ Electrolyte: Li ₃ PO _x Se _x	W × L: 20 × 50 μm	± 1.5 V	1 s	2.1–40.6 nS	(0.12) 0.1	(1.33/–0.34) 1.2/0.3	–	720 pulses	[47]
Channel: WO ₃ Electrolyte: LiClO ₄ –PVA + graphene	W × L: 10 × 100 μm t _{channel} : 30 nm	± 3 V	5 ms spaced by 1 s	0.8–22 μS	(0.26) –0.1	(0.99/–0.11) 0.4/0.3	–	500 pulses	[35]
Channel: WO ₃ Electrolyte: LiPON	W × L: 300 × 300 nm	± 100 pA	1 s	≈0.5–24 nS 1000 states	0	0.3/0.1	10 pJ (μm ² × nS) ^{–1}	10 ⁵ pulses	[46]
O²⁻-based devices									
Channel: WO _{3-x} Electrolyte: HfO ₂	L × W: 100 × 100 μm t _{ch} : 15 nm t _{el} : 10 nm	+4/–3 V	1 s	0.05–5.6 μS	(0.235)	(–0.09/0.16)	–	2000 pulses	[83]
Channel: WO ₃ Electrolyte: HfO _x	L × W: 10 × 4–40 μm t _{ch} : 4.5 nm t _{el} : 20 nm	+8/–6 V	200 μs	1–679 nS	0.4	1.8/–0.3	–	1000 pulses	[68]
Channel: WO _{2.7} Electrolyte: ZrO _{1.7}	L × W: 50 × 50 μm t _{ch} : 25 nm t _{el} : 40 nm	+4/–3.5 V	0.5 s	400 nS–1 μS 500 states	0.2	1.3/–1.4	–	1000 s 1000 pulses	[84]
Channel: TiO _{2-x} Electrolyte: YSZ Operated at 160 °C	W × L: 250 × 8000 μm t _{ch} : 60 nm t _{el} : 400 nm	± 1.5 V	2 μs	100–450 nS	0.1	1.9/1.2	10 aJ (μm ² × nS) ^{–1} Energy needed for heating is estimated to be ≈10 fJ per modulation event for (100 nm) ² devices.	3 × 10 ⁸ pulses 1 week	[65]
Channel: WO ₃ Electrolyte: YSZ	W × L: 10 × 5 μm	± 1 V	10 ms + 1 s delay	495–580 nS 100 states	0.4	(1.6/0.25)	–	10 ³ pulses 10 ³ s	[61]
Channel: Pr _{0.7} Ca _{0.3} MnO ₃ Electrolyte: HfO _x	W × L: 20 × 50 μm t _{ch} : 15 nm t _{el} : 20 nm	+3/–3.75 V	1 s	5–200 nS 100 states	0.1	1.5/0	–	4000 pulses 100 s	[85]
Channel: WO ₃ Electrolyte: HfO ₂	W × L: 100 × 100–10 × 4 μm	± 4 V	10 s–100 ns 10 ns	1.5–16 μS 1.58–1.61 μS	0.1 0	2.2/–0.2 0.3/2.6	10 pJ (μm ² × nS) ^{–1}	2 × 10 ⁷ pulses 14 h	[62]

Table 1. Continued.

Materials	Dimensions	Operating voltage	Pulse width	Dynamic range and number of analog states	Symmetry ^{a)}	Linearity ^{a)}	Energy consumption ^{b)}	Endurance/retention	Reference
Organic/polymer devices based on H⁺									
Channel: PEDOT:PSS Electrolyte: Nafion	L × W: 45 μm × 125 μm	± 650 mV	50 μs	50 nS–33 μS 50 states ΔG ² /σ ² = 91	0.1	3.1/–0.4	–	10 ⁸ pulses	[71]
Channel: p(g2T-TT) Electrolyte: EMIM:TFSI PVDF–HFP	W × L: 15 × 45 μm	± 1 V	20 ns	2–120 μS ΔG ² /σ ² > 100	0.1	1.2/0.3	0.1 aJ (μm ² × nS) ^{–1}	>10 ⁹ pulses at 90 °C Minutes	[73]
Channel: PEDOT:PSS Electrolyte: SiO ₂ + ionic liquid	L × W: 1–250 μm ²	± 1 V	100 + 200 ns delay	1–4 mS 100 states	0.3	4.8/–1.7	300 aJ (μm ² × nS) ^{–1}	10 ⁹ pulses	[75]
Channel: PEDOT:PSS Electrolyte: Nafion	L × W: 10 ^{–3} mm ²	± 0.5 mV	6 ms	600 μS–2 mS 500 states	0.3	4.5/–3.6	0.13 aJ (μm ² × nS) ^{–1}	5750 pulses 25 h	[70]
Inorganic devices based on H⁺									
Channel: WO ₃ Electrolyte: Nafion	W × L: 0.6 × 1.2 mm ²	200 nA	5 ms	2 μS–100 S 1000 states	0.1	0.5/0.1	18 aJ (μm ² × nS) ^{–1}	20000 pulses	[39]
Channel: WO ₃ Electrolyte: PSG	L: 2–100 μm t _{ch} : 10 nm t _{el} : 10 nm	± 3 V	1 s	0.6–0.8 μS	0.1	2.3/–3.3	2.2 fJ (μm ² × nS) ^{–1}	50000 pulses	[77]
Channel: WO ₃ Electrolyte: PSG	W × L: 50 × 150 nm t _{el} : 10 nm	+10/–8.5 V	5 ns	11–230 nS	0.1	0.7/0.1	3 fJ (μm ² × nS) ^{–1}	10 ⁵ pulses 100 s	[26]
Channel: WO ₃ Electrolyte: Si–H + hBN	W × L: 10 μm × 5–100 μm	± 1 V	10 ms	8–11 μS	–0.1	(0.9/0.9) 0.2/1.1	–	10 ⁵ pulses 10 ³ s	[78]
Devices using 2D materials									
Channel: 2D Ti ₃ C ₂ T _x MXene Electrolyte: H ₂ SO ₄ –PVA Working ion: H ⁺	W × L: 1000 × 20 μm	± 1 V	4 + 1 μs delay	1.6–2.8 mS 50 states ΔG ² /σ ² > 100	0.2 0.3	2.3/–2.0 0.3/2.3	13 aJ (μm ² × nS) ^{–1}	>10 ⁸ pulses 5 min	[80]
Channel: graphene Electrolyte: LiClO ₄ in PEO Working ion: Li ⁺	L × W: 3 × 12 μm t = 3 nm	± 3 V ± 50 pA	200 ns + 1 μs delay 10 ms	0.1–0.9 mS 250 states	0.2	1.1/0	1 aJ (μm ² × nS) ^{–1}	13 h	[79]
Other									
Channel: WO _x Electrolyte: HfO ₂ Working ion: Cu	W × L: 4–100 × 100 μm t _{ch} : 20 nm t _{el} : 25–45 nm	± 6 V	10 ms	240–300 μS 50 states	0.2	–	–	–	[86]
Typical values for state-of-the-art devices using alternative technologies									
Phase change memory	<1.8 nm	Tens to hundreds of microamperes	Tens of nanoseconds	1 μS–1 mS 2–3 states	–	–	10 pJ bit ^{–1}	10 ⁸ cycles 10 years	[87–89]
Resistive random access memory	<5 nm	1–2 V	10 ns	1 μS–1 mS 2–5 states	–	–	0.1 pJ bit ^{–1}	10 ¹² cycles 10 years	[88,89]

^{a)}Symmetry (AR) and linearity (α) quantitative descriptors as defined in Section 3 are calculated based on fitting data extracted from literature plots. This data extraction and fitting process limits the accuracy of these values, and thus they should only be taken as a general guide. Furthermore, only one representative plot was chosen from each literature report for the calculations, and symmetry/linearity values may vary from plot to plot depending on the number of states and conductance range traversed. Reported values are provided when available in parentheses (); ^{b)}Energy consumption has been normalized by L² × ΔG where data are available.

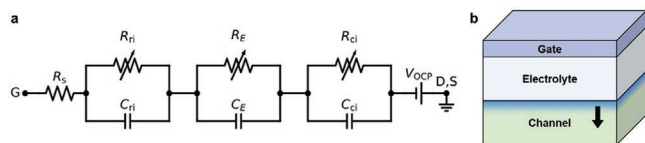


Figure 9. a) Equivalent circuit model for electrochemical ionic synapses. C_{ri} , C_{ci} and R_{ri} , R_{ci} represent the double-layer capacitances and the Faradaic resistances, respectively, at interfaces. C_E and R_E represent the bulk capacitance and the ion transport resistance of the electrolyte. V_{OCP} is the open-circuit potential of channel versus reservoir, and R_s represents the contact resistance. b) Ion redistribution in the channel after a gate voltage/current pulse intercalating ions into the channel. The color gradient indicates that the ion concentration in the channel is higher near the channel–electrolyte interface after the pulse. The arrow indicates the direction of ion redistribution in the channel by diffusion.

where j_x is the reaction current density, j_{x0} is the exchange current density, and α_x is the charge transfer coefficient for interface x , F is the Faraday constant, R is the ideal gas constant, z is the ion charge number, and V_x is the overpotential at interface x . Other charge-transfer models at interfaces^[95] can be adopted if future work finds them more appropriate. In the simulations that follow and for simplicity, the values of j_{x0} , and α_x for both interfaces are set to be the same and are denoted as j_0 and α , respectively.

The capacitors are the electrical double-layer (EDL) capacitors representing the hybrid capacitive ion/electron accumulation at the interfaces. An often-taken assumption/simplification is that when a cation conducting solid electrolyte (SE) is used, $[M^{n+}]_{\text{electrolyte}}$ cannot vary spatially within SE, because it is a line compound (thus would be punished severely in free energy when storing excess $[M^{n+}]_{\text{electrolyte}}$), and because the anions cannot move in SE and one has to maintain local electroneutrality. If so, the M^{n+} flux from reservoir \rightarrow SE must be equal to the M^{n+} flux from SE \rightarrow channel, since the solid electrolyte can only transport M^{n+} but not store it so the net number of anions inside does not change by decomposition. When this assumption is not true, for example, with a liquid electrolyte where the salt anions can also move (thus, one can build up a concentration gradient inside the electrolyte), one can still show that this equality holds as long as the electrons and all ions except M^{n+} are blocked, and the electrolyte is within its electrochemical stability voltage window. Then, we can have $\int_{\text{channel}+} dV\Delta[M] = -\int_{\text{reservoir}+} dV\Delta[M] = Q_{\text{ext}}/nF$, where $\Delta[M]$ is the change in the concentration of M , and Q_{ext} is the electronic charge that flows through the external circuit, if we take “channel+” and “reservoir+” regions to include the channel/electrolyte interface and reservoir/electrolyte interface regions with their EDL and ion segregation structure, respectively. In other words, in addition to $\Delta M_{\text{channel}} \leftrightarrow \Delta M^{n+}_{\text{channel}} + (\Delta n)e^-_{\text{channel}}$ in the bulk, we also need to add the ionic–electronic hybrid capacitive M^{n+}/e^- (or their anion or hole “deficit” versions) at the interface, into $\int_{\text{channel}+} dV\Delta[M]$. That is to say, the external electronic circuit drives dynamic doping of the channel bulk plus charging of its adjacent EDL where there can be excess M^{n+}/e^- also.

As a simplification, the voltages on the interfacial components are taken to be the overpotentials of the electrode, instead of the electrode potentials. The open-circuit potential, arising from the electrochemical potential of ions in the channel layer versus the reservoir layer is represented separately as a voltage component (V_{OCP}). This simplification introduces errors when

the equilibrium electrode potentials change during the simulation, but the errors are negligible when the OCP changes are small or when the chemical capacitance of the electrode is much larger than the EDL capacitances, which is the case in our simulations below. The value of V_{OCP} is determined by the concentrations of ions in each layer. For example, Yao et al. reported V_{OCP} values for an EIS with H_xWO_3 channel and PdH_x gate, as a function of the concentration of H in H_xWO_3 .^[39] A distributed-element equivalent circuit including chemical capacitance and diffusion elements can be constructed for the electrodes as discussed in ref. ^[96] for intercalation batteries. In our model, instead of using a distributed-element circuit, V_{OCP} is calculated by solving diffusion equation over space and time (discussed below), that is equivalent to the distributed-element circuit.

Finally, R_s is the total series electrical resistance of the gate stack. The equivalent circuit described here can be connected with external circuit components such as voltage and current sources, resistors, capacitors, and transistors to control the operation of an electrochemical ionic synapse in a given architecture.

The Faraday current at the electrodes inserts ions into or extracts ions from the channel layer, and the ions diffuse through the thickness of the channel layer over time (Figure 9b). Such a process is modeled by the diffusion equation

$$\frac{\partial c}{\partial t} = \frac{\partial}{\partial z} \left(D \frac{\partial c}{\partial z} \right) \quad (6)$$

where c is the concentration of ions in the channel, z is the coordinate along the channel thickness direction, and D is the ionic diffusivity in the channel material which is a function of ion concentration c .

Finally, the channel conductance G is calculated by

$$G = \frac{W}{L} \int_0^{t_c} \sigma(c(z)) dz \quad (7)$$

where t_c is the channel thickness, W is the channel width, L is the channel length, and σ is the electronic conductivity of the channel material, which is a function of c . The dependence of σ on c is determined by the channel material, the ion involved, and c itself. For example, when the dopant donates its electrons to in-gap states of a transition metal in an oxide channel material, σ increases with increasing c .

5.2. Validation of the Model Using Experimental Data

We validated this model with experimental data from different H^+ -based EIS devices, including our devices with the Nafion^[39] and the PSG electrolytes.^[77] For devices with Nafion electrolyte, we assume $\sigma_E = 0.09 \text{ S cm}^{-1}$,^[39] $j_0 = 10^{-5} \text{ A cm}^{-2}$, $\alpha = 0.5$, $C_e = 5 \text{ nF cm}^{-2}$, $C_i = 10 \text{ } \mu\text{F cm}^{-2}$, $z = 1$, $R_s = 200 \text{ } \Omega$, $L = 100 \text{ } \mu\text{m}$, $W = 500 \text{ } \mu\text{m}$, $t_c = 50 \text{ nm}$, $t_e = 400 \text{ nm}$. The ion-concentration-dependent parameters, V_{OCP} , D , and σ are taken from ref. ^[39]. The simulated results (Figure 10a) are in good agreement with the experimental results. The model captures a larger initial rate of depression upon reversal of the gate current polarity.

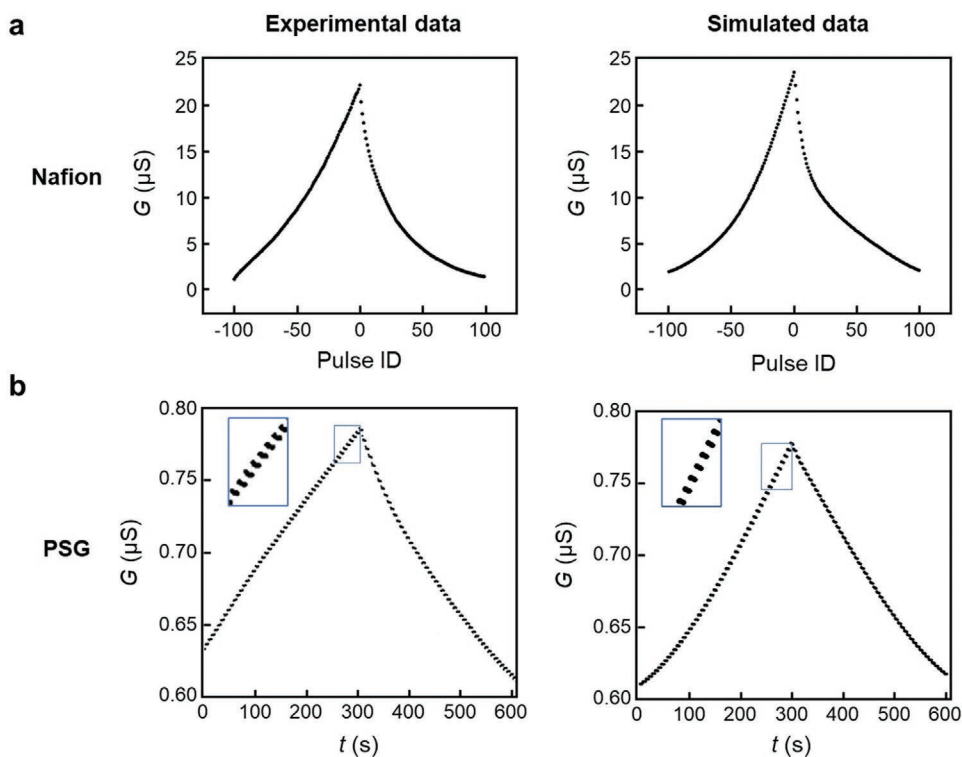


Figure 10. Experimental (left) and simulated (right) potentiation/depression data from EIS devices, showing reasonable agreement between the experimental result and model predictions. a) Potentiation/depression behavior of devices with WO_3 channel and Nafion electrolyte, applying 5 ms, $\pm 0.5 \mu\text{A}$ pulses with 1 s open-circuit intervals between pulses. Adapted with permission.^[39] Copyright 2020, The Authors, published by Springer Nature. b) Potentiation/depression behavior of devices with WO_3 channel and PSG electrolyte, applying 1 s, $\pm 3 \text{ V}$ voltage pulses with 5 s open-circuit intervals between pulses. Insets are the zoomed-in channel conductance traces close to the end of the potentiation pulses (highlighted by the rectangles in the plots). Adapted with permission.^[77] Copyright 2021, American Chemical Society.

For devices with PSG electrolyte,^[77] we assume $\alpha = 0.5$, $C_e = 0.1 \mu\text{F cm}^{-2}$, $C_i = 10 \mu\text{F cm}^{-2}$, $R_s = 10 \text{ k}\Omega$, $L = 10 \mu\text{m}$, $W = 5 \mu\text{m}$, $t_c = 10 \text{ nm}$, and $t_e = 10 \text{ nm}$. V_{OCP} and D are taken from ref. ^[39]. The WO_3 channel material is oxygen-deficient due to the atomic layer deposition method used in ref. ^[77], so the initial electronic conductivity is significantly higher than the WO_3 reported in ref. ^[39], and thus the conductivity has a lower modulation depth when inserting ions. This is modeled as an offset and scaling of the channel conductivity: $\sigma_{\text{oxygen-deficient WO}_3} = \sigma_{\text{stoichiometric WO}_3}/15.8 + 2.53 \text{ S cm}^{-1}$. In addition, the channel conductance calculation includes an addition of fixed $0.88 \text{ M}\Omega$ resistor in series to account for the channel region that is not under the gate. The field enhancement of ion conductivity of the 10 nm PSG electrolyte is considered by assuming the ion hopping distance $l_x = 0.6 \text{ nm}$.^[97] We found that a range of σ_0 values could achieve good agreement with the experimental potentiation/depression data by varying j_0 . We assume that j_0 varies between 10^{-15} and $10^{-3} \text{ A cm}^{-2}$, so that j_0 is not far below reported values for ion intercalation reactions at interfaces between electrodes and solid-state electrolytes (10^{-13} – $10^{-2} \text{ A cm}^{-2}$).^[98] With this assumption, the field-free proton conductivities, σ_0 , on the order of 10^{-11} – $10^{-10} \text{ S cm}^{-1}$ for PSG represent well the present data for potentiation and depression of the EIS device. This σ_0 range of the PSG electrolyte is lower than those reported in the literature, which studied PSG in humid environments as electrolyte for fuel cells.^[99,100] We attribute this

deviation to potential dehydration of PSG due to exposure to a gas environment with a low water partial pressure during measurement. The exact value of σ_0 and the reason for its deviation from earlier reported values require further investigation. Because the potentiation/depression behavior is not sensitive to the exchange current density (j_0), the capacitance (C_e , C_i), and the series resistances (R_s), these parameters cannot be extracted only from the reported experimental results. Further measurements are required to determine their exact values. Nonetheless, the simulation shows good agreement with the experimental result (Figure 10b), and captures the downward drift of the channel conductance between pulses during potentiation, as seen in the insets of Figure 10b. The postpulse relaxation could be caused by the ion redistribution in the channel, as will be discussed in Section 5.4.3.

5.3. EIS Operation Modes and Device Dynamics

The model described above provides insights into the EIS device operation modes, energy and size scaling, and dynamic response from complex waveforms such as pulse pairs. Below, we apply this model to compare a nonvolatile operation mode where the gate is open circuit in between pulses, and a volatile operation mode where the gate is connected to a resting voltage. An analysis of the energy consumption in the nonvolatile

operation mode (open circuit between pulses) is provided. In addition, the model predicts that the effect of the pulse pairs depends on the interval between pulses. The predictions also illustrate the potential of applying the electrochemical devices to mimic bioinspired dynamics such as spike-time-dependent plasticity (STDP), using ionic dynamics that are intrinsic to the EIS. Furthermore, when combined with extra circuit components, the model provides insights into the channel conductance drift of the EIS that arises from an electronic leakage path, which can be purposefully engineered to mimic the time-dependent forgetting behavior of biological systems.

The analysis below is applicable for EIS devices in general, including all types of ions that can be considered, including protons, lithium, oxygen, and others. The simulations aim to illustrate the generic behaviors of EIS devices using hypothetical but reasonable ranges of parameters, and are not carried out for any specific ion or material. The detailed device responses such as the amplitude of conductance changes and the timescales are expected to vary with different choices of material properties and device operation procedures.

5.3.1. Nonvolatile and Volatile Operation Modes

The operation of the EIS includes two stages to consider: the pulses for programming, and the electrical configuration when the pulses are off. Current pulsing and voltage pulsing are two commonly applied approaches for programming the electrochemical ionic synapses. Current-pulse operation potentially offers good symmetry and linearity because the operation is decoupled from the effect of open-circuit potential.^[39] However, it is challenging to implement current pulses in a crossbar array configuration. Voltage-pulse operations have shown similar performance with carefully chosen voltage and materials,^[23,38] and it is straightforward to implement in a crossbar array. In the following sections, we use voltage pulses to program the devices.

The electrical configuration when the pulse is off is also an important aspect of the EIS operation. We distinguish between two different configurations: 1) the open-circuit mode in which the gate is left open circuit, floating, and 2) the resting-potential mode in which the gate is connected to a fixed resting voltage (V_{rest}) after each pulse. In principle, these two configurations can also be combined for a targeted application.

To demonstrate the difference between the two postpulse configurations, we apply the model to study the response of a prototypical device (Figure 11). The simulations assume $j_0 = 10^{-5} \text{ A cm}^{-2}$, $\sigma_0 = 3 \times 10^{-10} \text{ S cm}^{-1}$, $L = W = 50 \text{ nm}$, σ from ref. ^[39], and other parameters to be the same as the PSG electrolyte device in Section 5.2. A 0.5 ms, +1 V pulse is applied to the gate to two identical devices at $t = 0$, and one device is left floating, open circuit, while the other device is connected to a rest potential which is the same as the open-circuit potential of the initial state at $t = 0$ ($V_{\text{rest}} = V_{\text{OCP}}^0$) immediately after the pulse. $V_{\text{rest}} = V_{\text{OCP}}^0$ ensures that the initial states of both devices are equivalent because no current is flowing through the gate in either device before the pulse applications. The channel conductance dynamics in a long timescale (120 s) are shown in Figure 11a, inset. In the open-circuit mode, the channel conductance shows a nonvolatile increase. As described ear-

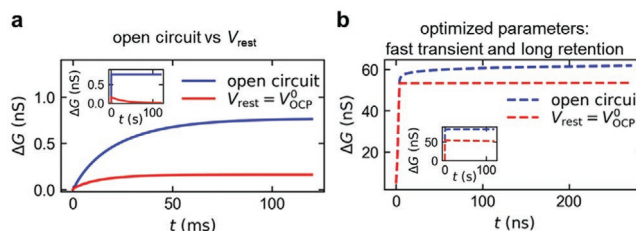


Figure 11. Two modes of EIS configuration after a voltage pulse: open-circuit mode (blue) and resting potential mode (red) between pulses. a) The conductance change (ΔG) as a function of time (t) for the two modes after applying the same 0.5 ms, 1 V pulse, showing t from 0 to 120 ms. Inset, the same plot showing t from 0 to 120 s. b) ΔG as a function of t for the two modes, assuming $j_0 = 10^{-7} \text{ A cm}^{-2}$, $\sigma_0 = 10^{-7} \text{ S cm}^{-1}$, after applying a 5 ns 12 V pulse. The difference in conductance changes is smaller between the two modes, and a quick settling is achieved for the resting potential mode. Inset, ΔG as a function of t from 0 to 120 s, showing long retention in resting potential mode.

lier, when the circuit is open, the electrons and ions cannot go back from the channel to the reservoir. On the other hand, the increase of the channel conductance is volatile when the EIS device is in the resting potential mode, which is set to $V_{\text{rest}} = V_{\text{OCP}}^0$ right after the pulse. In this mode, ions and electrons re-equilibrate to the concentration in the channel and reservoir consistent with the initial electrochemical potential of the device; that is, ions and electrons flow back to the reservoir from the channel, and thus, the channel conductance evolves back overtime toward the initial value. Such volatile behavior has been seen in ref. ^[65].

The volatile behavior of the EIS devices is dictated by the thermodynamics of such a battery-like closed system electrochemical devices. The EIS device is in essence a battery, and applying a rest potential between the reservoir and the channel is equivalent to connecting a battery to a constant voltage, which generally drives the system toward a fixed charge state that equilibrates with that potential. For an EIS device, the fixed charge state corresponds to a fixed conductance state at equilibrium. As a result, the EIS device connected to a constant voltage will forget the effect of the prior pulses equilibrated with a new charge state at the chosen rest potential, and thus we have the volatile behavior of the device.

Keeping the device at a chosen rest potential does not need to be zero OCP. Rest potential can be any potential that we choose to set as a reference state. Zero OCP necessitates that the chemical potential of hydrogen in the reservoir electrode and in the channel electrode is the same. It is possible to achieve this, for example, by symmetric electrodes with the same hydrogen concentration to start with.

In addition to the difference in volatility, the device in the resting potential mode has a smaller channel conductance change than the device in the open-circuit mode. This is because when the device is connected to V_{OCP}^0 right after a pulse application, the negative gate current generated by the V_{OCP}^0 partially reverses the effect of the voltage pulse. Figure 11a shows that it takes a longer time for the channel conductance to be stabilized in the open-circuit mode. The longer delay is due to the slow intercalation of ions into the channel after being built up at the electrode–electrolyte interface capacitance during the

pulse. However, when the device is connected to V_{OCP}^0 , the negative gate current after the pulse reduces the ionic charge in the capacitors, resulting in a smaller conductance change after the pulse is off.

Both the volatile behavior and the differences in amplitude can be optimized by changing the material parameters and the operation conditions, as shown in Figure 11b. By assuming $j_0 = 10^{-7} \text{ A cm}^{-2}$, $\sigma_0 = 10^{-7} \text{ S cm}^{-1}$, $t_{\text{pulse}} = 5 \text{ ns}$, and $V_{\text{pulse}} = 12 \text{ V}$, simulations show that the amplitude of ΔG from the resting potential mode is comparable to the open-circuit mode, a long retention can be achieved in resting potential mode, and the conductance settles quickly assuming instantaneous redistribution of ions through the thickness of the channel.

Compared to the resting potential mode, the open-circuit mode enables larger conductance change for the same pulse because all charge flow through the gate is utilized for intercalation of dopant to the channel, and therefore has higher energy efficiency. The resting potential mode charges and discharges the capacitors resulting in excess energy consumptions. The open-circuit mode also has a longer retention time, in principle infinite. In addition, the open-circuit mode takes longer time for the channel conductance to stabilize, due to charge accumulation at the electrode–electrolyte interfaces.

In crossbar arrays, if EIS devices are directly connected to the row and column lines that supply voltage signals, the operation of each EIS is in resting potential mode because the gate is always connected to a voltage source. If an additional selector component is integrated with each EIS device, the gate can be set to open circuit when the selector is off, so open-circuit mode can be realized. The additional selector component may increase the integration complexity and device area.

Because open-circuit mode enables nonvolatile operation with low energy consumption, in the following sections, we use the open-circuit mode as the operation configuration to derive the material properties for the purpose of achieving the desired specifications.

5.3.2. Energy Consumption Scaling versus Device Geometry and Pulse Voltage

The energy consumption (E) associated with ion migration and interactions by voltage pulses can be calculated by multiplying the pulse voltage (V_{pulse}) with the amount of charge that flows through the gate during the pulse (q_{pulse})

$$E = V_{\text{pulse}} q_{\text{pulse}} \quad (8)$$

If the electrolyte is assumed to be insulating to electronic charge carriers and the device is left open circuit after the pulse, all ions that flow through the stack get inserted into the channel. As a result, the charge that flows through the gate is directly related to the number of ions inserted into the channel

$$q_{\text{pulse}} = z q_e n_{\text{ions}} \quad (9)$$

where z is the charge number of ions being inserted (number of electrons associated with each ion insertion/extraction for

charge neutrality), q_e is the electron charge, and n_{ions} is the number of ions that are inserted for each pulse.

Because the inserted ions modulate the channel conductivity, n_{ions} should be determined by the targeted values of ΔG for each pulse. To calculate n_{ions} , we assume that each pulse only causes a very small concentration change of ions in the channel (Δc), so that the change of channel conductivity ($\Delta \sigma$) can be approximated by a linear relation

$$\Delta \sigma = \Delta c \frac{d\sigma}{dc} \quad (10)$$

where $\frac{d\sigma}{dc}$ is the sensitivity of conductivity to the ion concentration for the channel material. This linear approximation gives

$$\Delta c = \Delta \sigma \left(\frac{d\sigma}{dc} \right)^{-1} \quad (11)$$

The desired $\Delta \sigma$ is determined by the targeted ΔG and the channel geometry

$$\Delta \sigma = \Delta G \frac{L}{W t_c} \quad (12)$$

Substituting Equation (12) into Equation (11) gives

$$\Delta c = \Delta G \frac{L}{W t_c} \left(\frac{d\sigma}{dc} \right)^{-1} \quad (13)$$

Then, n_{ions} can be calculated by

$$n_{\text{ions}} = \Delta c W L t_c \quad (14)$$

Substituting Equation (14) into Equations (8) and (9) gives

$$E = V_{\text{pulse}} z q_e \Delta G L^2 \left(\frac{d\sigma}{dc} \right)^{-1} \quad (15)$$

Equation (15) shows that the energy consumption of a voltage pulse is proportional to the pulse voltage, and the square of the channel length, and inversely proportional to the sensitivity of the electronic conductivity of the channel material to the ion concentration, $\frac{d\sigma}{dc}$. The sensitivity is determined by the mechanism of electronic conductivity modulation in the channel, and it may vary with the ion concentration.

To demonstrate the energy consumption calculation for a device with WO_3 channel, the σ versus c dependence is assumed to be as reported in ref. [39], the channel geometry is set as $W = L = 50 \text{ nm}$, $t_c = 10 \text{ nm}$ and the initial ion concentration ($x \approx 0.04$ in H_xWO_3 , in the low G regime in ref. [39]) is chosen such that the resistance is $24 \text{ M}\Omega$, and the change of channel conductance (0.16 nS) corresponding to a $100 \text{ k}\Omega$ change in the channel resistance. The energy consumption is then calculated to be 4.4 aJ per pulse at $V_{\text{pulse}} = 1 \text{ V}$. This corresponds to 28 singly charged ions per pulse, such as H^+ .

The energy consumption as a function of the pulse voltage and the length of the channel is shown in Figure 12. The

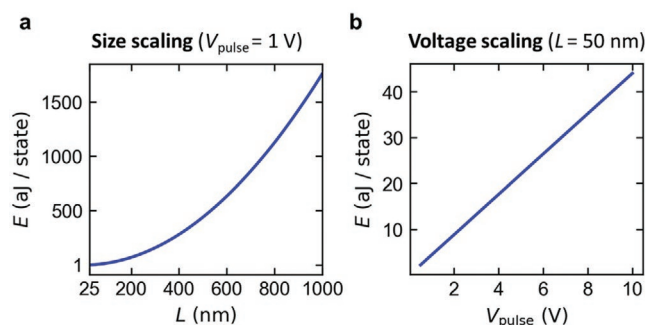


Figure 12. Energy scaling of an EIS device with a WO_3 channel and $W:L=1:1$, in order to achieve a ΔG of 0.16 nS that corresponds to a 100 k Ω change in resistance, starting from 24 M Ω . a) Energy per pulse versus channel length for 1 V. b) Energy per pulse versus pulse voltage for a device with a channel length of 50 nm to achieve a 0.16 nS change in channel conductivity.

analysis shows that reducing the operating voltage, and the channel length are effective approaches to reducing the energy consumption. Hence, devices that are CMOS compatible are favorable as they can leverage existing fabrication processes for size miniaturization. A low operation voltage (below ≈ 1 V) is favorable for achieving low energy consumption. However, lower gate voltage for programming provides a smaller driving force for ion transport and charge transfer reactions, and thus slower rates of these processes and slower devices. Achieving fast modulation and fast settling at low operation voltage demands electrolyte materials with fast ion conductivity and interfaces with fast charge transfer kinetics, and the quantitative targets are deduced in Section 5.4 below.

5.3.3. Response from Consecutive Pulses

To illustrate the temporal dynamics of the EIS device, two simulations are carried out with pulse pairs that consist of the same 70 ns, +2.5 V voltage pulses, but separated by different time

delays ($\Delta t = 500$ ns and $\Delta t = 10$ μs). The simulations assume $j_0 = 10^{-5}$ A cm^{-2} , $\sigma_0 = 2 \times 10^{-5}$ S cm^{-1} , $L = W = 50$ nm, σ from ref. [39], instantaneous redistribution of ions through the thickness of the channel, and other parameters to be the same as the PSG electrolyte device in Section 5.2. The time delays are chosen such that the electrolyte capacitor is close to fully re-equilibrated in between pulses. The devices are set to $V_{\text{rest}} = 0$ V when the pulse is off.

When the two pulses are separated by a long delay (Figure 13a, blue line), the net ΔG of the pulse pair is close to double of that from a single pulse (Figure 13b, blue line). However, when the two pulses are applied with a short delay, the pulse pair induces a larger ΔG (Figure 13b, red line). The difference in ΔG induced by different pulse delays can be explained by the difference in the charging state of the interfacial double-layer capacitors (V_c) at the onset of the second pulse, as shown in Figure 13c. The rate of ion and electron insertion into the channel is determined by V_c through Equation (5). When the delay between two pulses is short, the value of V_c is not able to recover to the equilibrium value, so the second pulse increases it to a higher value than the peak value from the first pulse. Because the reaction current is exponentially dependent on V_c , the resulting ΔG is much enhanced. The shorter pulse intervals resulted in larger conductance modulation, as shown in Figure 13d (blue line). If the channel conductance is also modulated by the double-layer charging state, the transient double-layer voltage can also be observed from the channel conductance as a volatile component. This could explain the reported experimental results of devices showing an enhanced volatile channel conductance change by pulse pairs with short intervals.^[48,101,102] The results suggest the potential for EIS devices to mimic paired pulse facilitation (PPF) in biological systems where the postsynaptic response is larger from the second than from the first pulse.^[103] Finally, when the pulse polarity of the two pulses is reversed, so that one pulse is positive, and the other is negative, a different dependence of ΔG versus Δt is observed (Figure 13e, blue line). Such behavior can potentially be utilized to mimic STDP in neuroscience-inspired applications. Because the double-layer

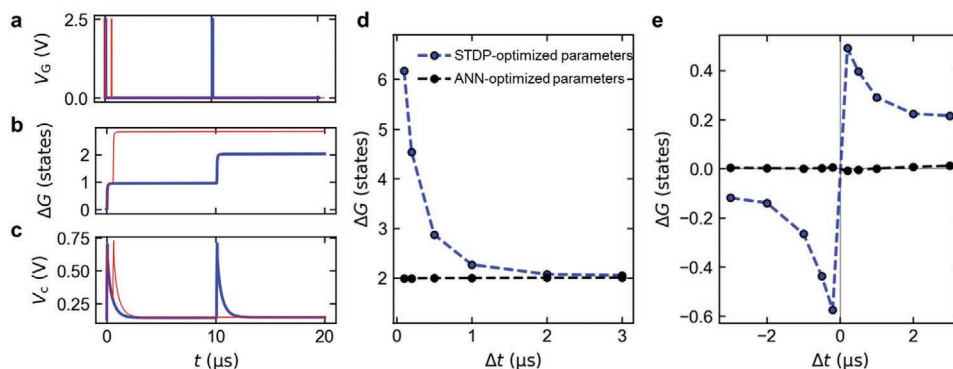


Figure 13. Dependence of conductance change from pulse pairs on pulse intervals. a–c) The gate voltage V_G (a), conductance change ΔG (b), and channel–electrolyte interface potential V_c (c) as a function of time (t) from the application of two 70 ns, 2.5 V voltage pulses separated by either 10 μs (blue) or 0.5 μs (red) of delay. ΔG is larger when the interval between the two pulses (Δt) is smaller. The device is short-circuited (0 V) when the pulse is off. d) ΔG after the pulse pair versus Δt for simulations with parameters the same as (a–c) (blue) optimized for capturing STDP, and with parameters optimized for implementing analog neural networks (black, $j_0 = 0.1$ A cm^{-2} , $\sigma_0 = 10^{-7}$ S cm^{-1} , $V_{\text{pulse}} = 12$ V, $t_{\text{pulse}} = 5$ ns). e) ΔG after the pulse pair versus Δt . The pulse pair consists of two 70 ns pulses with $V_{\text{pulse}} = 2.5$ and -3.16 V for simulations with the same parameters as (a–c) (blue), and consists of two 5 ns pulses with $V_{\text{pulse}} = 12$ and -12.6 V (black). The negative pulse is applied first when Δt is negative.

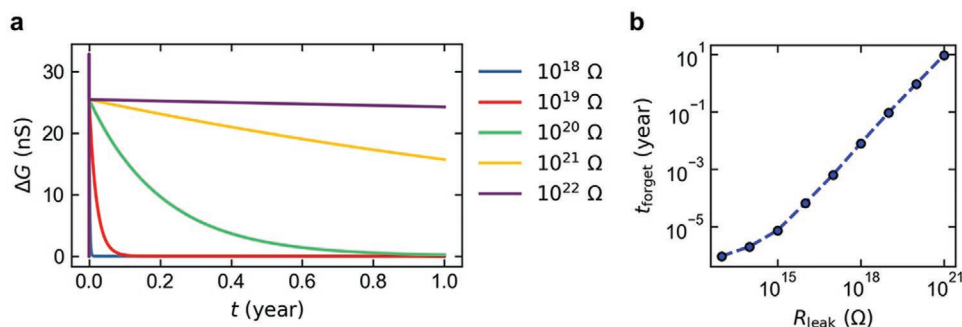


Figure 14. Controllable long-time forgetting behavior with a leaky resistor connected in parallel with the EIS device (this can also be obtained by a leaky electrolyte within the device). a) The conductance change versus time after a 2 V, 50 ns pulse, showing the conductance decay as a function of resistance of the leaky parallel resistor, ranging from short to very long times of decay (forgetting). b) The time of forgetting (t_{forget}) the synaptic weight change as a function of the resistance of the parallel resistor.

capacitance dynamics depend on the charge transfer reaction rate at the interface, the timescale where interactions between consecutive pulses are relevant can be engineered by choice of materials. The interactions between the pulses can be minimized by varying the material properties and the operation procedures, as seen in Figure 13d,e (black lines). The minimum interactions between consecutive pulses is desirable to achieve linear weight updates for implementing analog neural network crossbars.^[25]

Electrochemical ionic synapses are conventionally treated as programmable resistors, the state of which can be fully described by the channel conductance. With this simplified view, the same voltage or current pulse is expected to change the channel conductance by the same amount if the device has the same initial channel conductance state. However, here we show that this simplified view may be inaccurate. The model suggests that state variables (such as V_c) that depend on the history of the electrochemical synapses, here the time delay between each pulse, have an effect on the resulting conductance behavior of the devices. Additional state variables worth consideration are the ion concentration distribution in the channel, the local temperature profile, and the aging of materials. In order to achieve predictable and consistent conductance update for ANN computations using pulses with short intervals, it is important to take such factors into consideration because the ΔG from multiple pulses may differ from the sum of ΔG expected from individual pulses.

5.3.4. Controllable Forgetting

If the electrolyte has no electronic conductivity, and there is no external current flowing, ΔG is nonvolatile and the conductance change stays forever, as there is no electronic path for reversing the electrochemical reactions, as discussed in Section 5.3.1. The nonvolatility is beneficial for storing information in the long term. However, it is possible to introduce a leakage path purposefully to mimic a time-dependent forgetting behavior similar to that in biological systems. Here, we show that with a symmetric device (WO_3 as both the reservoir and channel materials), the forgetting time (t_{forget} , time to recover 99% of the conductance change) can be tuned from seconds to years depending

on the resistance of a leak resistor connecting the reservoir and the channel in parallel to the electrochemical synapse circuit (Figure 14). The simulations assume $j_0 = 10^{-5} \text{ A cm}^{-2}$, $\sigma_0 = 2 \times 10^{-5} \text{ S cm}^{-1}$, $L = W = 100 \text{ nm}$, σ from ref. [39], and other parameters to be the same as the PSG electrolyte device in Section 5.2. Alternatively, the electronic conductivity (leakiness) of the electrolyte layer in the device can also serve the purpose of the leak resistor and achieve controlled forgetting.

5.4. Material Requirements for Achieving the Desired Device Performance Specifications

In the following sections, we present the use of the EIS device model to deduce material properties needed for any given ion, for achieving the desired specifications of fast modulation, fast settling, low voltage, and low energy consumption operation, as outlined in Section 3. In particular, we are interested in identifying the electrolyte ion conductivity and electrolyte-channel and electrolyte-reservoir interface charge transfer reaction rates that enable the programming of the EIS devices with at most 1 V, 10 ns pulses, and response and settling times less than 300 ns. The material requirements calculated here are applicable for EIS devices using any monovalent ion, because the equations governing the processes in these systems are the same. In addition, the model may not be applicable when the electric field in the electrolyte is close to the breakdown strength, because electronic leakage of the electrolyte under high electric field is not considered. The simulations below are operating at low voltage (1 V) and low electric field conditions, so that the electrolyte is electronically insulating.

5.4.1. Nanosecond Pulse Operation and Fast Modulation Transient

We first define the programming dynamics characterized by three timescales, t_{pulse} (the duration of the pulse needed to achieve the desired final conductance change ΔG_{final}), $t_{80\%}$ (the time needed to achieve 80% of ΔG_{final}), and t_{settle} (the time it takes before ΔG stays within the 5% error band of ΔG_{final}), as shown in Figure 15a. As an example, a 50 μs , 5 V pulse is applied to a device at $t = 0$, and the conductance transient is

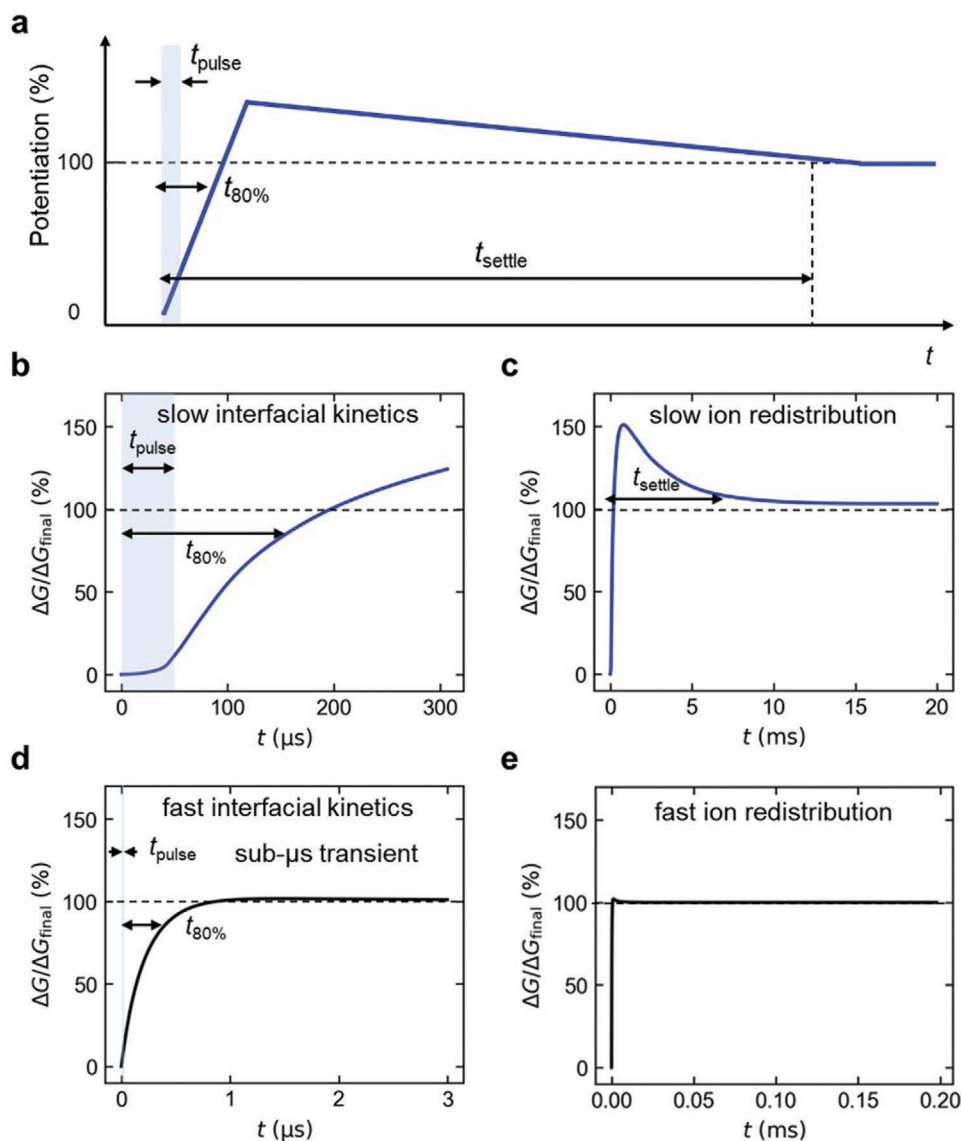


Figure 15. a) Schematic illustration of the channel conductance from a voltage pulse applied to the gate showing t_{pulse} , $t_{80\%}$, and t_{settle} . b) Example of device channel conductance dynamics from 0 to 300 μs when a 50 μs , 5 V pulse is applied at $t = 0$. t_{settle} is the time needed for the channel conductance to stay within 5% of the final conductance value. c) The same channel conductance dynamics as (a), from 0 to 20 ms. d,e) The channel conductance dynamics with $j_0 = 1 \text{ A cm}^{-2}$, $\sigma_0 = 10^{-7} \text{ S cm}^{-1}$, $V_{\text{pulse}} = 1.5 \text{ V}$, $t_{\text{pulse}} = 10 \text{ ns}$, showing short pulse duration (10 ns) and sub-microsecond transients.

shown in Figure 15b,c. The simulations assume $j_0 = 10^{-5} \text{ A cm}^{-2}$, $\sigma_0 = 3 \times 10^{-10} \text{ S cm}^{-1}$, $L = W = 50 \text{ nm}$, σ from ref. [39], and other parameters to be the same as the PSG electrolyte device in Section 5.2. The operation conditions and model parameters are chosen so that the conductance dynamics can be separately observed at different timescales. The plot for the short timescale (Figure 15b, 0–300 μs) shows that the potentiation is not complete when the pulse stops, as the conductance only changes by around 25% of the final value within the pulse duration.

The channel conductance reaches 80% of the final conductance change at $t_{80\%} \approx 0.15 \text{ ms}$, which is ≈ 3 times the pulse duration. The delay is due to the slow kinetics of charge transfer at the channel–electrolyte interface following the charging of the channel–electrolyte interface capacitance during the pulse.

In the final stage, the conductance keeps increasing beyond 100% of the final value, followed by a relaxation of the conductivity down toward the final value till t_{settle} of $\approx 7 \text{ ms}$, as shown in Figure 15c. The conductivity relaxation is due to the higher concentration of ions near the interface and the nonlinear dependence of channel conductivity on the ion concentration. The t_{settle} of $\approx 7 \text{ ms}$ is long after the pulse. Long transients after the pulse may contribute to delay or inaccuracy in subsequent training and inferences. The channel conductance dynamics is controlled by the material properties and the operation procedures. Fast pulse (10 ns) and sub-microsecond settling can be achieved by material optimizations such as shown in Figure 15d,e.

To provide a guideline for material optimizations, we will study t_{pulse} , $t_{80\%}$, and t_{settle} when operated at $V_{\text{pulse}} = 1 \text{ V}$ (desirable operation voltage as discussed in Section 3). t_{pulse} needed for a

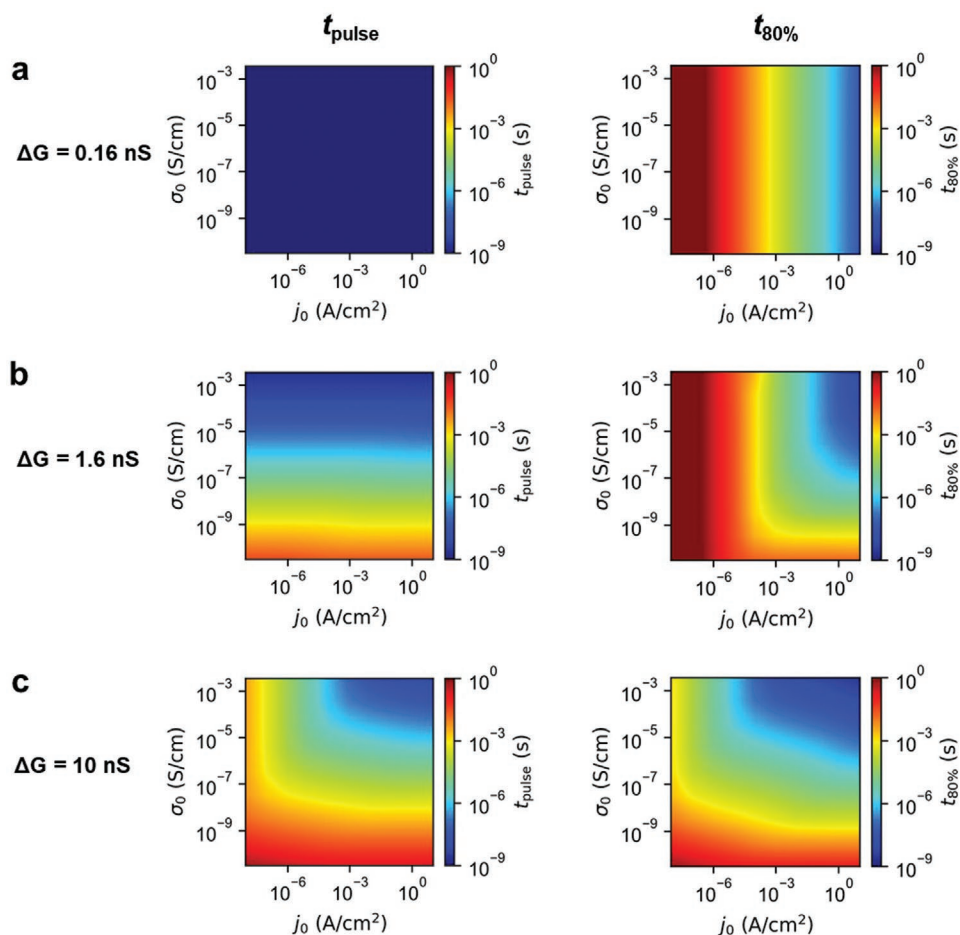


Figure 16. a–c) Effect of electrolyte ionic conductivity σ_0 and the exchange current density of the electrodes (j_0) on the speed of electrochemical ionic synapses, characterized by t_{pulse} (left) and $t_{80\%}$ (right), when the target conductivity change (ΔG) per pulse is 0.16 nS (a), 1.6 nS (b), and 10 nS (c), covering the range of ΔG values suggested in Section 3.

certain conductance change per state and $t_{80\%}$ depend primarily on the ionic conductivity of the electrolyte σ_E and the exchange current density j_0 at the electrode–electrolyte interface. t_{settle} depends on the ion redistribution by diffusion in the channel. The conductivity of the electrolyte σ_E depends on the field, so we instead study the effect of its value at the low field limit, σ_0 . Under $V_{\text{pulse}} = 1$ V, the electric field inside the 10 nm thick electrolyte is ≈ 1 MV cm $^{-1}$ maximum, under which the ionic conductivity is enhanced only by a factor of 0.28 \times . We first focus on the t_{pulse} and $t_{80\%}$, assuming instantaneous ion redistribution in the channel material. As discussed in Section 3, a range of ΔG per state can potentially be desirable, ranging from 0.1 nS (for 1000 states with a minimum resistance of ≈ 10 M Ω), to 10 nS (for 100 states with a minimum resistance of ≈ 1 M Ω). Depending on the desired ΔG per pulse, we identify three regimes with representative conductance change values ($\Delta G = 0.16$, 1.6, and 10 nS) and the dependence of the timescales on the material properties for each regime is shown in Figure 16.

When the required conductance change is small ($\Delta G = 0.16$ nS) (Figure 16a), sub-nanosecond t_{pulse} is needed, regardless of the ionic conductance and the interface material. t_{pulse} is not sensitive to either σ_0 or j_0 . This is because the voltage pulse redistributes the ions in the electrolyte C_E into

the interface C_{ci} , which provides enough ions (≈ 28 protons) to achieve the required conductance change. Such ion redistribution from the electrolyte capacitance to the interface needs very short-range redistribution of ions near the interface, and thus, it is fast and does not depend on σ_0 or j_0 . When the ions are driven to the channel–electrolyte interface, more time is needed for charge transfer reactions at the interface, which transfers ions and electrons into the channel, to reach the final conductance value. The time needed for this process (characterized by $t_{80\%}$) depends on the charge transfer rate of the interfaces (Figure 16a). A fast interface charge transfer rate ($j_0 = 1$ A cm $^{-2}$) is needed to achieve fast potentiation ($t_{80\%} \approx 300$ ns). After each pulse, the electrolyte capacitor is charged, and in order to get the same amount of ion redistribution for the next pulse, the electrolyte capacitor needs to be re-equilibrated. The re-equilibration process depends on ion transport through the electrolyte, which is proportional to σ_0 , so the time needed for re-equilibration (t_{eq}) is shorter for higher σ_0 (Figure 17). In order to achieve consistent operations for pulses with 10 ns intervals, an ionic conductivity on the order of 10^{-4} S cm $^{-1}$ is needed.

Figure 16b shows the dependence of t_{pulse} and $t_{80\%}$ on material properties, when the required conductance change is in an intermediate range ($\Delta R = 1$ M Ω , or $\Delta G = 1.6$ nS). On one hand,

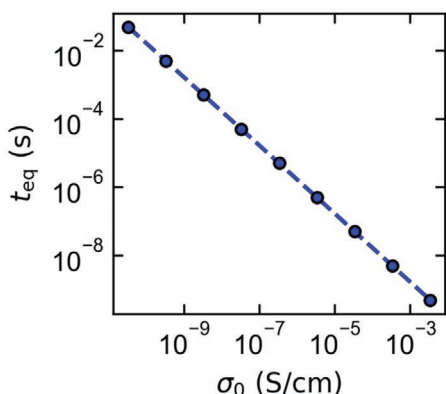


Figure 17. Time to re-equilibrate the electrolyte capacitor by 80% (t_{eq}) versus the field-free ionic conductivity σ_0 . The effect of electrolyte capacitor re-equilibration can be ignored, if ΔG per pulse is much larger than the conductance change induced by the ions from electrolyte capacitance.

the ions needed for the desired ΔG is around 4 times larger than what the electrolyte capacitor can provide at 1 V, so the potentiation process requires ion transport through the electrolyte. As a result, t_{pulse} depends on the ionic conductivity of the electrolyte. On the other hand, the number of ions needed is still small so that the voltage drop on the channel–electrolyte interface is small (≈ 0.35 V) compared to the gate voltage (1 V), so the majority of the gate voltage is applied on the electrolyte regardless of the interface kinetics. As a result, t_{pulse} is insensitive to the change of interface kinetics. In this regime, $\sigma_0 \approx 10^{-4}$ S cm $^{-1}$ is needed for 10 ns pulse operations. Similar to the first regime, $t_{80\%}$ is dependent on the interface kinetics j_0 . To achieve a $t_{80\%}$ of 300 ns, $j_0 \approx 0.1$ A cm $^{-2}$ is needed, which is lower than the required j_0 value in the first regime due to the speed enhancement from a higher interface voltage drop.

Figure 16c shows the dependence of t_{pulse} and $t_{80\%}$ on material properties, when the required conductance change is large (10 nS). Due to the large change of the conductance, the potentiation process not only requires charging the interface capacitors, but also requires enough ions to be intercalated through R_{ci} during the pulse. In this regime, t_{pulse} depends on both σ_0 and j_0 . $t_{80\%}$ is shorter than t_{pulse} , which indicates that the majority of the potentiation happens during the pulse, so the dependence of $t_{80\%}$ on σ_0 and j_0 follows t_{pulse} . In this regime, both a high proton conduction ($\sigma_0 \approx 10^{-3}$ S cm $^{-1}$) and a fast charge transfer rate ($j_0 \approx 1$ A cm $^{-2}$) are needed for 10 ns pulse operations.

In summary, in all of these operation regimes, in order to achieve repeatable operation with fast pulse and fast rise of conductance within 300 ns, a fast ionic conductivity $\sigma_0 \approx 10^{-4}$ – 10^{-3} S cm $^{-1}$ and fast interfacial kinetics $j_0 \approx 0.1$ – 1 A cm $^{-2}$ are needed. We note that the predicted material properties are applicable to any ion of choice to work within the EIS.

5.4.2. Rate Limiting Processes

Identifying the rate limiting processes in an EIS device helps to resolve the bottleneck of the performance, as the performance can be improved effectively when the rate limiting process is

accelerated. The rate limiting processes can be determined from plots such as those in Figure 16, which show the dependence of t_{pulse} and $t_{80\%}$ on σ_0 and j_0 . At any point on the plot, if the equal color contour is vertical, the response in question is not sensitive to σ_0 , but to j_0 , so the interfacial reactions are the rate limiting process. Conversely, if the equal color contour is horizontal, the ion conduction is identified as the rate limiting process. When the equal color contour is neither horizontal nor vertical, the timescale depends on both σ_0 and j_0 , and both processes are comparable in determining the response rate of the EIS device. The rate limiting conditions depend on the values of the material properties, as well as operation conditions such as the pulse voltage and the amplitude of the conductance change per pulse.

5.4.3. Postpulse Relaxation due to Ion Redistribution in the Channel

Above, we have studied the pulse duration and the time needed to insert the desired amount of ions into the channel, while assuming instantaneous diffusion in the channel material. As discussed above in Section 5.4.1, the postpulse conductance transient response is further affected by ion redistribution in the channel. The effect of ion redistribution is modeled by solving the diffusion equation (Equation (6)) over space and time, and the conductance is calculated by Equation (7). Such postpulse conductance transient from the ion redistribution is attributed to the diffusion of ions in the channel from the channel–electrolyte interface to the bulk of the channel material, and the nonlinear dependence of conductivity of the channel material on the ion concentration.

To demonstrate the effect of ion redistribution in the channel on the dynamics of conductance change, the devices with both high σ_0 and j_0 ($\sigma_0 = 10^{-3}$ S cm $^{-1}$, $j_0 = 1$ A cm $^{-2}$) are used for simulation. For simplicity, D is assumed to be a constant and does not vary with c . When ion redistribution in the channel is instantaneous, a pulse of 1 V is applied to change the channel resistance by ≈ 100 k Ω . The rise time ($t_{80\%}$) is within ≈ 300 ns (Figure 18a, yellow line), consistent with Figure 16a. However, when the diffusion and redistribution of the ions within the channel layer are considered (Figure 18a, blue line), it takes $t_{settle} > 0.2$ ms for the conductance to settle to the desired values with a D value of 10^{-12} cm 2 s $^{-1}$. This additional delay is due to the redistribution of ions in the channel, from the electrolyte–channel interface to the depth of the channel layer, as seen in Figure 18b. The concentration change near the interface is much larger than that of the final concentration change, so the linear approximation in Equation (10) no longer holds, and the nonlinear dependence of conductivity on the concentration causes the channel conductance to depend on the distribution of ions in the channel. With higher D values, both the timescale and the amplitude of the deviations from the final ΔG are reduced. As shown in Figure 18a and inset, at $D = 10^{-8}$ cm 2 s $^{-1}$, the deviation becomes negligible. If the ion conduction and the interfacial reaction kinetics are fast, so that the ion intercalation is instantaneous, t_{settle} is inversely proportional to D , as shown in Figure 18c. The exact channel conductance transient also depends on the nonlinearity of the channel conductivity versus

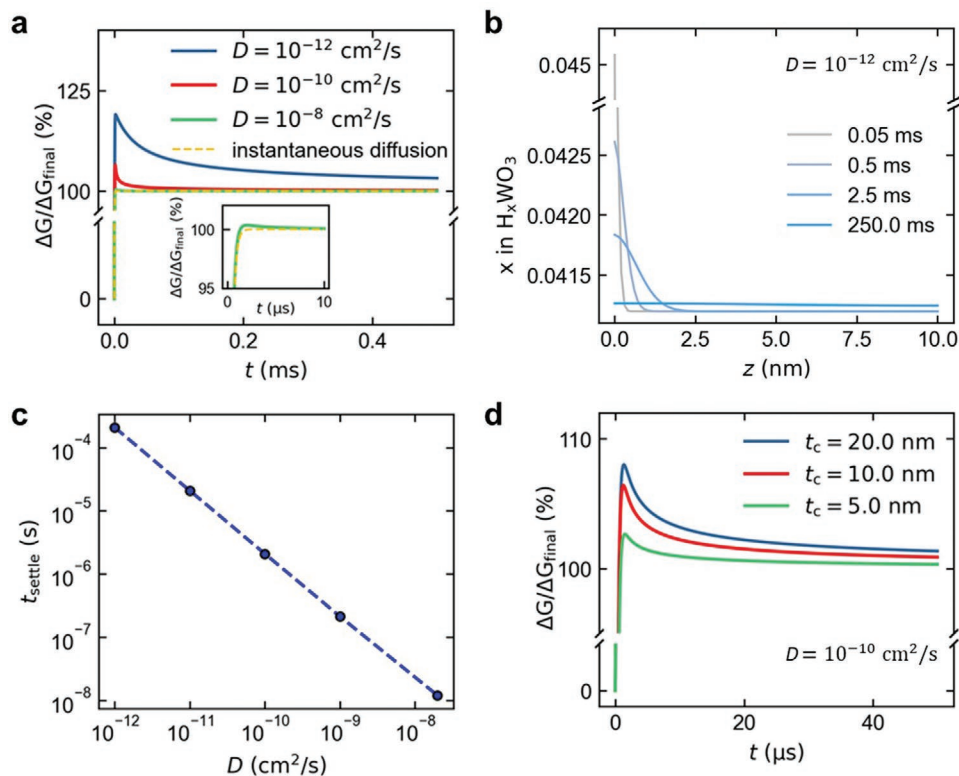


Figure 18. Redistribution of ions in the channel after a voltage pulse. a) The channel conductance change (ΔG) versus time for different diffusivities (D). Inset, the zoomed-in plot at $t = 0$ – $10 \mu\text{s}$ showing that the effect of ion redistribution is negligible for $D = 10^{-8} \text{ cm}^2 \text{ s}^{-1}$. b) x in H_xWO_3 as a function of time and z -location in the channel, showing the intercalation of hydrogen into the channel happens first at the interface and then diffuses through the thickness of the channel over time. c) t_{settle} as a function of D assuming the ion intercalation is instantaneous. d) ΔG versus time for different channel thicknesses (t_c).

the ion concentrations, and the amplitude of the concentration change near the interface. A D value for ions in the channel at least on the order of $\approx 10^{-8}$ – $10^{-9} \text{ cm}^2 \text{ s}^{-1}$ is needed to achieve a settling time ≈ 300 ns or less from ion redistribution in the channel.

To decrease this postpulse relaxation time, channel materials with fast ion diffusion can be adapted. A smaller channel thickness will also reduce the characteristic timescale for the redistribution, as seen in Figure 18d. Finally, the channel conductance is less affected by the redistribution if the conductivity is highly linear with respect to the ion concentration.

5.5. Predicted Material Properties for Targeted Operations

From the model simulations, we have extracted the material properties needed for achieving the targeted specifications in Section 3, specifically programming with 1 V pulses and with $\Delta G = 0.1$ – 10 nS between each state. The model shows that, for an EIS device with a 10 nm thick solid-state electrolyte, and a 10 nm channel with electronic conductivity as reported in ref. [39], an ionic conductivity of 10^{-4} – $10^{-3} \text{ S cm}^{-1}$, and an interfacial exchange current density of 0.1–1 A cm⁻² are needed to achieve 10 ns pulse operations with a rise time < 300 ns. In addition, an ion diffusivity of 10^{-8} – $10^{-9} \text{ cm}^2 \text{ s}^{-1}$ in the channel material

is needed to ensure the channel conductance change from dopant redistribution settles within ≈ 300 ns. The diffusivity requirement could be relaxed if the channel is thinner or if the channel material has an electronic conductivity that is linearly dependent on the ion concentration.

6. Conclusion and Outlook

Electrochemical ionic synapses, also commonly referred to as electrochemical random access memories, present an exciting potential for application in ANN acceleration due to their repeatability, good linearity, and symmetry with low energy consumption. A wide variety of material systems including Li⁺-based, O²⁻-based, and H⁺-based systems have been studied. However, the desired specifications of fast operation (nanosecond) at low voltage (1 V) simultaneously in a given device have not been met yet. By using the electrochemical circuit model of EIS devices, we have identified the desirable material properties to achieve fast and low voltage operation for any given ion. We next discuss potential strategies and challenges toward meeting these requirements. In addition, array level integration with large array size has not been demonstrated so far. It would be beneficial to perform array-level integration studies as proof of concept toward practical applications of

the devices in AI workloads. Moreover, there are opportunities beyond achieving ANN computations with these devices. It is possible to harvest the ionic dynamics in these devices for neuromorphic computations that involve time-domain information processing and advanced bioplausible computation.

6.1. Target Materials toward Desirable Device Specifications

While electrochemical ionic synapses show great promise for accelerating artificial intelligence workloads, there are challenges that need to be addressed. Although a fast modulation speed of ≈ 5 ns has been demonstrated,^[46,62] devices with simultaneously large conductance modulation range ($\approx 10\times$, 100–1000 states), low operation voltage (≈ 1 V), fast programming, and fast settle time have not been reported. As discussed in Section 5.5, to achieve fast programming time at low voltage, the ionic conductivity of the electrolyte, the electrochemical reaction kinetics, and ion diffusion in the channel need to be high ($\sigma_0 \approx 10^{-4}$ – 10^{-3} S cm⁻¹, $j_0 \approx 0.1$ – 1 A cm⁻², and $D \approx 10^{-8}$ – 10^{-9} cm² s⁻¹). Nevertheless, these target material properties do not yet exist simultaneously in electrolyte and channel material classes that are compatible with CMOS and with BEOL processes. However, there are promising material classes that have the potential to be engineered to deliver the targeted material and device properties.

To improve ionic conduction in the electrolyte, materials with higher ionic conductivity at room temperature need to be developed. Extensive studies have been carried out to improve the ionic conductivity of Li⁺, H⁺, and O²⁻ electrolytes for lithium batteries and solid oxide fuel cells (SOFCs),^[104–107] and this knowledge and strategies can be leveraged to design and optimize electrolyte materials for electrochemical ionic synapses. While SOFCs usually operate at elevated temperatures, electrochemical ionic synapses are usually expected to operate at near room temperature. As a result, room temperature operation should be emphasized in the material design and research of oxygen ion and proton conductors.

In particular, proton conduction in solid-state electrolytes at low temperature (<50–150 °C) can benefit from absorbed and surface-bound water, which provides a boost in proton conductivity.^[108] Enhanced proton conduction around room temperature has been reported widely in porous oxides such as YSZ,^[109–111] ceria,^[112,113] titanium dioxide,^[114] and glasses.^[99,100] Proton conductivities of >1 mS cm⁻¹ have been reported for nanoporous anatase^[114] and PSG^[100] under high humidity conditions. The proton conductivity of these materials generally is sensitive to humidity. As a result, for the practical integration of such electrolytes, it is important to trap or encapsulate the water content so that the proton conductivity remains high and stable after the chip is packaged. The composite of sepiolite-phosphoric acid has been reported as a solid-state proton conductor with conductivity of 15 mS cm⁻¹ at room temperature,^[115] which is promising for application in electrochemical ionic synapses, but the deposition and processing of such films need to be studied. In addition to achieving high ionic conductivity, low electronic leakage is also an important factor for the material design of electrolyte, because electronic leakage increases the energy consumption and reduces retention. Finally, being compatible with microfabrication processes is important for

achieving a smaller footprint and convenient integration with CMOS components.

An alternative approach to improve ionic conduction is to reduce the thickness of the electrolyte. At the extreme of thickness scaling, monolayer 2D materials such as graphene and hBN have been shown to exhibit good proton conductivity.^[78,116] As the electrolyte layer becomes thinner, the high electric field from the gate voltage may enhance ionic conductivity. A concern could be the electronic leakage and breakdown of thinner electrolytes. The electronic conduction and breakdown mechanisms under strong field strength need to be understood for the optimization of very thin electrolytes.

In addition to ionic conduction through the electrolyte, the channel–electrolyte interface charge transfer reaction needs to be improved to ensure low overpotential and fast intercalation/extraction of ions. Insights into the electrode kinetics and engineering of the electrode–electrolyte interface are needed for the improvement of the charge transfer rate.

Channel materials should have a suitable range of conductance modulation, high sensitivity of conductivity to ion intercalation for efficient operation, and fast redistribution of ions for fast settling of the channel conductance. Low-dimensional nanomaterials are promising candidates as channel materials, because when the thickness of the channel becomes one atom thick, the ion redistribution in the devices is expected to settle instantaneously. Reversible ion intercalation into 2D materials can be achieved both through the edge of the 2D material laterally, and through the layers vertically,^[117] enabling both lateral and vertical gated designs.

The device structure is also important for improved performance of the electrochemical ionic synapses. Most devices reported so far have a planar transistor-like structure. Strategies from transistor designs such as gate-all-around (GAA) structure could potentially be explored. In a planar geometry, only one side of the channel is in contact with the electrolyte, while with device structures similar to fin field-effect transistors or GAA transistors, the ion transport and electrochemical reactions can happen from multiple sides of the channel, increasing the areas for ion transport and charge transfer reactions, and reducing the time needed for the ion redistribution in the channel.

6.2. Array and System Integration

There have been only a small number of studies that report integrated arrays of electrochemical ionic synapses, and the demonstrated array sizes are small (2×2 and 3×3)^[62,71,84] compared to the demonstrated systems based on two-terminal resistive switching devices.^[118,119] Several key challenges need to be addressed for array integration. To build on top of standard CMOS circuits, the devices need to use only CMOS-compatible materials with BEOL-compatible processes. Devices based on H⁺ and Li⁺ need to be properly encapsulated with diffusion barrier materials to ensure prolonged device lifetime and reliable operation. Another challenge that needs to be addressed is the device-to-device variation as the device dimension is reduced. Smaller device area may also lead to stochasticity/variation due to the heterogeneities of microstructures. When the devices are in operation, the effect of

external conditions such as temperature variations also needs to be studied. The energy consumption, delay, and accuracy of an integrated system should be evaluated and optimized. Beyond crossbar arrays, biological brains benefit from the connectivity of 3D architecture and scaling. Exploring bottom-up fabrication methods such as self-assembly of nanomaterials^[120] may open up new possibilities in connectivity and lowering the cost of fabrication.

6.3. Neuroscience-Guided Computing

In addition to the ANN crossbar architecture, electrochemical ionic synapses have also shown the potential to efficiently replicate and mimic the dynamics observed in biological systems, including PPF and STDP,^[48,70,82,121] as shown here in Figure 13. Similar to biological synapses, the electrochemical ionic synapses rely on ions to function. Advances in neuroscience provides insights into the neural circuits and plasticity rules involved in learning certain tasks. These insights could inform the design of hardware circuits to emulate the learning rules, in which electrochemical ionic synapses serve as energy-efficient building blocks. It is still an open question as to what aspects of the biological system are important for specific computational tasks. Mimicking more complex dynamics in biological systems may come with higher costs in terms of energy consumption, device footprint, and complexity. An exciting perspective of electrochemical ionic synapses is that bioinspired learning rules can potentially be implemented utilizing the intrinsic ionic dynamics of the device with a reduced number of extra electronic components. For example, the strength of potentiation depends on the relative timing of pre- and postsynaptic firing and rate-dependent plasticity effects.^[48,70,82,121] In addition, different device configurations can be explored, such as multigate,^[82] and global/local signal^[122] for the emulation of complex control and global rewards. In order to fully realize the potential of such intrinsic dynamics, it is important to understand and develop models to gain insights into the dynamics, so that the transient responses of devices from various stimuli can be effectively predicted, and material guidelines can be provided for implementing biorealistic learning rules. Finally, given the involvement of ion dynamics both in the biological synapses and in the artificial electrochemical synapses, these devices and relevant circuits could, in return, become a platform for the modeling and validation of learning rules deduced from neuroscience studies.

Acknowledgements

M.H. and M.S. contributed equally to this work. This work was supported by the MIT Quest for Intelligence program, the MIT-IBM Watson AI Research Lab, and the Semiconductor Research Corporation (SRC) under Task #3010.001.

Conflict of Interest

The authors declare no conflict of interest.

Keywords

electrochemical ionic synapses, ion intercalation, neuromorphic engineering, programmable resistors

Received: June 8, 2022

Revised: September 13, 2022

Published online:

- [1] Y. LeCun, Y. Bengio, G. Hinton, *Nature* **2015**, 521, 436.
- [2] D. Silver, J. Schrittwieser, K. Simonyan, I. Antonoglou, A. Huang, A. Guez, T. Hubert, L. Baker, M. Lai, A. Bolton, Y. Chen, T. Lillicrap, F. Hui, L. Sifre, G. van den Driessche, T. Graepel, D. Hassabis, *Nature* **2017**, 550, 354.
- [3] J. Jumper, R. Evans, A. Pritzel, T. Green, M. Figurnov, O. Ronneberger, K. Tunyasuvunakool, R. Bates, A. Židek, A. Potapenko, A. Bridgland, C. Meyer, S. A. A. Kohl, A. J. Ballard, A. Cowie, B. Romera-Paredes, S. Nikolov, R. Jain, J. Adler, T. Back, S. Petersen, D. Reiman, E. Clancy, M. Zielinski, M. Steinegger, M. Pacholska, T. Berghammer, S. Bodenstein, D. Silver, O. Vinyals, et al., *Nature* **2021**, 596, 583.
- [4] J. D. Kelleher, *Deep Learning*, The MIT Press, Cambridge, MA, USA **2019**.
- [5] J. Shalf, *Philos. Trans. R. Soc., A* **2020**, 378, 20190061.
- [6] D. Amodei, D. Hernandez, G. Sastry, J. Clark, G. Brockman, I. Sutskever, "AI and Compute," **2019**.
- [7] A. Mehonic, A. J. Kenyon, *Nature* **2022**, 604, 255.
- [8] A. Sebastian, M. Le Gallo, R. Khaddam-Aljameh, E. Eleftheriou, *Nat. Nanotechnol.* **2020**, 15, 529.
- [9] Q. Xia, J. J. Yang, *Nat. Mater.* **2019**, 18, 309.
- [10] W. Zhang, B. Gao, J. Tang, P. Yao, S. Yu, M.-F. Chang, H.-J. Yoo, H. Qian, H. Wu, *Nat. Electron.* **2020**, 3, 371.
- [11] S. Ambrogio, P. Narayanan, H. Tsai, R. M. Shelby, I. Boybat, C. di Nolfo, S. Sidler, M. Giordano, M. Bodini, N. C. P. Farinha, B. Killeen, C. Cheng, Y. Jaoudi, G. W. Burr, *Nature* **2018**, 558, 60.
- [12] M. J. Marinella, S. Agarwal, A. Hsia, I. Richter, R. Jacobs-Gedrim, J. Niroula, S. J. Plimpton, E. Ipek, C. D. James, *IEEE J. Emerging Sel. Top. Circuits Syst.* **2018**, 8, 86.
- [13] H.-Y. Chang, P. Narayanan, S. C. Lewis, N. C. P. Farinha, K. Hosokawa, C. Mackin, H. Tsai, S. Ambrogio, A. Chen, G. W. Burr, *IBM J. Res. Dev.* **2019**, 63, 8:1.
- [14] Z. Wang, H. Wu, G. W. Burr, C. S. Hwang, K. L. Wang, Q. Xia, J. J. Yang, *Nat. Rev. Mater.* **2020**, 5, 173.
- [15] J. J. Yang, D. B. Strukov, D. R. Stewart, *Nat. Nanotechnol.* **2013**, 8, 13.
- [16] Y. Li, Z. Wang, R. Midya, Q. Xia, J. J. Yang, *J. Phys. D: Appl. Phys.* **2018**, 51, 503002.
- [17] S. Yu, X. Guan, H.-S. P. Wong, in *2011 Int. Electron Devices Meeting*, IEEE, Piscataway, NJ, USA **2011**, <https://doi.org/10.1109/IEDM.2011.6131572>.
- [18] S. Choi, S. H. Tan, Z. Li, Y. Kim, C. Choi, P.-Y. Chen, H. Yeon, S. Yu, J. Kim, *Nat. Mater.* **2018**, 17, 335.
- [19] K. M. Kim, J. J. Yang, J. P. Strachan, E. M. Grafals, N. Ge, N. D. Melendez, Z. Li, R. S. Williams, *Sci. Rep.* **2016**, 6, 20085.
- [20] F. Alibart, L. Gao, B. D. Hoskins, D. B. Strukov, *Nanotechnology* **2012**, 23, 075201.
- [21] J. Li, B. Luan, C. Lam, in *2012 IEEE Int. Reliability Physics Symp. (IRPS)*, IEEE, Piscataway, NJ, USA **2012**, <https://doi.org/10.1109/IRPS.2012.6241871>.
- [22] S. Thakoor, A. Moopenn, T. Daud, A. P. Thakoor, *J. Appl. Phys.* **1990**, 67, 3132.
- [23] E. J. Fuller, F. E. Gabaly, F. Léonard, S. Agarwal, S. J. Plimpton, R. B. Jacobs-Gedrim, C. D. James, M. J. Marinella, A. A. Talin, *Adv. Mater.* **2017**, 29, 1604310.
- [24] B. Chen, X. Wang, B. Gao, Z. Fang, J. Kang, L. Liu, X. Liu, G.-Q. Lo, D.-L. Kwong, *Sci. Rep.* **2015**, 4, 6863.

- [25] T. Gokmen, Y. Vlasov, *Front. Neurosci.* **2016**, *10*, 333.
- [26] M. Onen, N. Emond, B. Wang, D. Zhang, F. M. Ross, J. Li, B. Yildiz, J. A. del Alamo, *Science* **2022**, *377*, 539.
- [27] S. Agarwal, T.-T. Quach, O. Parekh, A. H. Hsia, E. P. DeBenedictis, C. D. James, M. J. Marinella, J. B. Aimone, *Front. Neurosci.* **2016**, *9*, 484.
- [28] T. Gokmen, M. Onen, W. Haensch, *Front. Neurosci.* **2017**, *11*, 538.
- [29] T. Gokmen, W. Haensch, *Front. Neurosci.* **2020**, *14*, 103.
- [30] T. Gokmen, *Front. Artif. Intell.* **2021**, *4*, 699148.
- [31] S. Agarwal, S. J. Plimpton, D. R. Hughart, A. H. Hsia, I. Richter, J. A. Cox, C. D. James, M. J. Marinella, in *2016 Int. Joint Conf. Neural Networks (IJCNN)*, IEEE, Piscataway, NJ, USA **2016**, pp. 929–938.
- [32] G. W. Burr, R. M. Shelby, S. Sidler, C. di Nolfo, J. Jang, I. Boybat, R. S. Shenoy, P. Narayanan, K. Virwani, E. U. Giacometti, B. N. Kurdi, H. Hwang, *IEEE Trans. Electron Devices* **2015**, *62*, 3498.
- [33] M. Prezioso, F. Merrih-Bayat, B. D. Hoskins, G. C. Adam, K. K. Likharev, D. B. Strukov, *Nature* **2015**, *521*, 61.
- [34] M. Onen, T. Gokmen, T. K. Todorov, T. Nowicki, J. A. del Alamo, J. Rozen, W. Haensch, S. Kim, *Front. Artif. Intell.* **2022**, *5*, 891624.
- [35] R. D. Nikam, M. Kwak, J. Lee, K. G. Rajput, H. Hwang, *Adv. Electron. Mater.* **2020**, *6*, 1901100.
- [36] J.-W. Jang, S. Park, G. W. Burr, H. Hwang, Y.-H. Jeong, *IEEE Electron Device Lett.* **2015**, *36*, 457.
- [37] D. B. Strukov, R. S. Williams, *Appl. Phys. A: Mater. Sci. Process.* **2009**, *94*, 515.
- [38] Y. Li, E. J. Fuller, S. Asapu, S. Agarwal, T. Kurita, J. J. Yang, A. A. Talin, *ACS Appl. Mater. Interfaces* **2019**, *11*, 38982.
- [39] X. Yao, K. Klyukin, W. Lu, M. Onen, S. Ryu, D. Kim, N. Emond, I. Waluyo, A. Hunt, J. A. del Alamo, J. Li, B. Yildiz, *Nat. Commun.* **2020**, *11*, 3134.
- [40] *Decadal Plan for Semiconductors*, Semiconductor Research Corporation, Durham, NC, USA **2021**.
- [41] R. C. Merkle, *Energy Limits to the Computational Power of the Human Brain*, Foresight Institute, Palo Alto, CA, USA **1989**.
- [42] S. B. Laughlin, R. R. de Ruyter van Steveninck, J. C. Anderson, *Nat. Neurosci.* **1998**, *1*, 36.
- [43] K. Kim, C.-L. Chen, Q. Truong, A. M. Shen, Y. Chen, *Adv. Mater.* **2013**, *25*, 1693.
- [44] L. Q. Zhu, C. J. Wan, L. Q. Guo, Y. Shi, Q. Wan, *Nat. Commun.* **2014**, *5*, 3158.
- [45] Y. H. Liu, L. Q. Zhu, P. Feng, Y. Shi, Q. Wan, *Adv. Mater.* **2015**, *27*, 5599.
- [46] J. Tang, D. Bishop, S. Kim, M. Copel, T. Gokmen, T. Todorov, S. Shin, K. Lee, P. Solomon, K. Chan, W. Haensch, J. Rozen, *IEEE Int. Electron Devices Meet.* **2018**, 13.1.1.
- [47] R. D. Nikam, M. Kwak, J. Lee, K. G. Rajput, W. Banerjee, H. Hwang, *Sci. Rep.* **2019**, *9*, 18883.
- [48] C.-S. Yang, D.-S. Shang, N. Liu, E. J. Fuller, S. Agrawal, A. A. Talin, Y.-Q. Li, B.-G. Shen, Y. Sun, *Adv. Funct. Mater.* **2018**, *28*, 1804170.
- [49] J. Lee, R. D. Nikam, S. Lim, M. Kwak, H. Hwang, *Nanotechnology* **2020**, *31*, 235203.
- [50] D. Young, A. Ransil, R. Amin, Z. Li, Y.-M. Chiang, *Adv. Energy Mater.* **2013**, *3*, 1125.
- [51] C. A. Marianetti, G. Kotliar, G. Ceder, *Nat. Mater.* **2004**, *3*, 627.
- [52] A. Milewska, K. Świerczek, J. Tobola, F. Boudoire, Y. Hu, D. K. Bora, B. S. Mun, A. Braun, J. Molenda, *Solid State Ionics* **2014**, *263*, 110.
- [53] T. Katase, T. Onozato, M. Hirono, T. Mizuno, H. Ohta, *Sci. Rep.* **2016**, *6*, 25819.
- [54] K. Yoshimatsu, T. Soma, A. Ohtomo, *Appl. Phys. Express* **2016**, *9*, 075802.
- [55] R. Baddour-Hadjean, S. Bach, M. Smirnov, J.-P. Pereira-Ramos, *J. Raman Spectrosc.* **2004**, *35*, 577.
- [56] Y. Hamon, A. Douard, F. Sabary, C. Marcel, P. Vinatier, B. Pecquenard, A. Levasseur, *Solid State Ionics* **2006**, *177*, 257.
- [57] B. Put, P. M. Vereecken, J. Meersschaut, A. Sepúlveda, A. Stesmans, *ACS Appl. Mater. Interfaces* **2016**, *8*, 7060.
- [58] J. Speulmanns, A. M. Kia, K. Kühnel, S. Bönhardt, W. Weinreich, *ACS Appl. Mater. Interfaces* **2020**, *12*, 39252.
- [59] A. M. Kia, J. Speulmanns, S. Bönhardt, J. Emara, K. Kühnel, N. Haufe, W. Weinreich, *Appl. Surf. Sci.* **2021**, *564*, 150457.
- [60] D. M. Bishop, P. Solomon, S. Kim, J. Tang, J. Tersoff, T. Todorov, M. Copel, J. Collins, K. T. Lee, S. Shin, W. Haensch, J. Rozen, in *Extended Abstracts 2018 Int. Conf. Solid State Devices Materials*, The Japan Society Of Applied Physics, Hongo Campus, The University of Tokyo, Tokyo, Japan **2018**.
- [61] R. D. Nikam, M. Kwak, H. Hwang, *Adv. Electron. Mater.* **2021**, *7*, 2100142.
- [62] S. Kim, T. Todorov, M. Onen, T. Gokmen, D. Bishop, P. Solomon, K.-T. Lee, M. Copel, D. B. Farmer, J. A. Ott, T. Ando, H. Miyazoe, V. Narayanan, J. Rozen, *IEEE Int. Electron Devices Meet.* **2019**, 35.7.1.
- [63] J. Shi, S. D. Ha, Y. Zhou, F. Schoofs, S. Ramanathan, *Nat. Commun.* **2013**, *4*, 2676.
- [64] H.-Y. Huang, C. Ge, Q.-H. Zhang, C.-X. Liu, J.-Y. Du, J.-K. Li, C. Wang, L. Gu, G.-Z. Yang, K.-J. Jin, *Adv. Funct. Mater.* **2019**, *29*, 1902702.
- [65] Y. Li, E. J. Fuller, J. D. Sugar, S. Yoo, D. S. Ashby, C. H. Bennett, R. D. Horton, M. S. Bartsch, M. J. Marinella, W. D. Lu, A. A. Talin, *Adv. Mater.* **2020**, *32*, 2003984.
- [66] Y. Li, W. C. Chueh, *Annu. Rev. Mater. Res.* **2018**, *48*, 137.
- [67] N. Rösemann, K. Ortner, J. Petersen, T. Schadow, M. Bäker, G. Bräuer, J. Rösler, *Surf. Coat. Technol.* **2015**, *276*, 668.
- [68] H. Kwak, C. Lee, C. Lee, K. Noh, S. Kim, *Semicond. Sci. Technol.* **2021**, *36*, 114002.
- [69] J. Rivnay, S. Inal, A. Salleo, R. M. Owens, M. Berggren, G. G. Malliaras, *Nat. Rev. Mater.* **2018**, *3*, 17086.
- [70] Y. van de Burgt, E. Lubberman, E. J. Fuller, S. T. Keene, G. C. Faria, S. Agarwal, M. J. Marinella, A. Alec Talin, A. Salleo, *Nat. Mater.* **2017**, *16*, 414.
- [71] E. J. Fuller, S. T. Keene, A. Melianas, Z. Wang, S. Agarwal, Y. Li, Y. Tuchman, C. D. James, M. J. Marinella, J. J. Yang, A. Salleo, A. A. Talin, *Science* **2019**, *364*, 570.
- [72] A. Gumyusenge, A. Melianas, S. T. Keene, A. Salleo, *Annu. Rev. Mater. Res.* **2021**, *51*, 47.
- [73] A. Melianas, T. J. Quill, G. LeCroy, Y. Tuchman, H. v Loo, S. T. Keene, A. Giovannitti, H. R. Lee, I. P. Maria, I. McCulloch, A. Salleo, *Sci. Adv.* **2020**, *6*, eabb2958.
- [74] S. T. Keene, A. Melianas, Y. van de Burgt, A. Salleo, *Adv. Electron. Mater.* **2019**, *5*, 1800686.
- [75] Y. Tuchman, T. J. Quill, G. LeCroy, A. Salleo, *Adv. Electron. Mater.* **2021**, *8*, 2100426.
- [76] J. Lee, S. Lim, M. Kwak, J. Song, H. Hwang, *Nanotechnology* **2019**, *30*, 255202.
- [77] M. Onen, N. Emond, J. Li, B. Yildiz, J. A. del Alamo, *Nano Lett.* **2021**, *21*, 6111.
- [78] R. D. Nikam, J. Lee, W. Choi, W. Banerjee, M. Kwak, M. Yadav, H. Hwang, *Small* **2021**, *17*, 2103543.
- [79] M. T. Sharbati, Y. Du, J. Torres, N. D. Ardolino, M. Yun, F. Xiong, *Adv. Mater.* **2018**, *30*, 1802353.
- [80] A. Melianas, M.-A. Kang, A. VahidMohammadi, T. J. Quill, W. Tian, Y. Gogotsi, A. Salleo, M. M. Hamedi, *Adv. Funct. Mater.* **2021**, *32*, 2109970.
- [81] A. VahidMohammadi, J. Rosen, Y. Gogotsi, *Science* **2021**, *372*, eabf1581.
- [82] M. Kumar, U. Kim, W. Lee, H. Seo, *Adv. Mater.* **2022**, *34*, 2200122.
- [83] Y. Jeong, H. Lee, D. G. Ryu, S. H. Cho, G. Lee, S. Kim, S. Kim, Y. S. Lee, *Adv. Electron. Mater.* **2021**, *7*, 2100185.
- [84] J. Lee, R. D. Nikam, M. Kwak, H. Hwang, *ACS Appl. Mater. Interfaces* **2022**, *14*, 13450.
- [85] C. Lee, K. G. Rajput, W. Choi, M. Kwak, R. D. Nikam, S. Kim, H. Hwang, *IEEE Electron Device Lett.* **2020**, *41*, 1500.
- [86] H. Kang, H. W. Kim, E. R. Hong, J. Woo, *Appl. Phys. Lett.* **2022**, *120*, 122101.

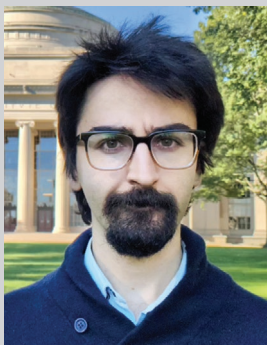
- [87] B. Liu, K. Li, W. Liu, J. Zhou, L. Wu, Z. Song, S. R. Elliott, Z. Sun, *Sci. Bull.* **2021**, *66*, 2217.
- [88] E. I. Vatajelu, P. Pouyan, S. Hamdioui, *Int. J. Circuit Theory Appl.* **2018**, *46*, 4.
- [89] R. Islam, H. Li, P.-Y. Chen, W. Wan, H.-Y. Chen, B. Gao, H. Wu, S. Yu, K. Saraswat, H.-S. P. Wong, *J. Phys. D: Appl. Phys.* **2019**, *52*, 113001.
- [90] B.-Y. Chang, S.-M. Park, *Annu. Rev. Anal. Chem.* **2010**, *3*, 207.
- [91] P. Vadhva, J. Hu, M. J. Johnson, R. Stocker, M. Braglia, D. J. L. Brett, A. J. E. Rettie, *ChemElectroChem* **2021**, *8*, 1930.
- [92] I. G. Austin, M. Sayer, *J. Phys. C: Solid State Phys.* **1974**, *7*, 905.
- [93] A. Heuer, S. Murugavel, B. Roling, *Phys. Rev. B* **2005**, *72*, 174304.
- [94] E. J. F. Dickinson, A. J. Wain, *J. Electroanal. Chem.* **2020**, *872*, 114145.
- [95] G. Zhang, K. Guo, X. Shen, H. Ning, H. Liang, J. Zhong, W. Xu, B. Tang, R. Yao, J. Peng, *ACS Appl. Mater. Interfaces* **2021**, *13*, 4768.
- [96] J. Jamnik, J. Maier, *Phys. Chem. Chem. Phys.* **2001**, *3*, 1668.
- [97] R. A. B. Devine, G. V. Herrera, *Phys. Rev. B* **2001**, *63*, 233406.
- [98] R. Amin, I. Belharouak, *J. Power Sources* **2017**, *348*, 318.
- [99] M. Nogami, R. Nagao, C. Wong, *J. Phys. Chem. B* **1998**, *102*, 5772.
- [100] M. Nogami, R. Nagao, C. Wong, T. Kasuga, T. Hayakawa, *J. Phys. Chem. B* **1999**, *103*, 9468.
- [101] J. Zhu, Y. Yang, R. Jia, Z. Liang, W. Zhu, Z. U. Rehman, L. Bao, X. Zhang, Y. Cai, L. Song, R. Huang, *Adv. Mater.* **2018**, *30*, 1800195.
- [102] C. S. Yang, D. S. Shang, N. Liu, G. Shi, X. Shen, R. C. Yu, Y. Q. Li, Y. Sun, *Adv. Mater.* **2017**, *29*, 1700906.
- [103] R. S. Zucker, W. G. Regehr, *Annu. Rev. Physiol.* **2002**, *64*, 355.
- [104] Q. Zhao, S. Stalin, C.-Z. Zhao, L. A. Archer, *Nat. Rev. Mater.* **2020**, *5*, 229.
- [105] C. Wang, K. Fu, S. P. Kammampata, D. W. McOwen, A. J. Samson, L. Zhang, G. T. Hitz, A. M. Nolan, E. D. Wachsman, Y. Mo, V. Thangadurai, L. Hu, *Chem. Rev.* **2020**, *120*, 4257.
- [106] S. Hossain, A. M. Abdalla, S. N. B. Jamain, J. H. Zaini, A. K. Azad, *Renewable Sustainable Energy Rev.* **2017**, *79*, 750.
- [107] V. Kharton, F. Marques, A. Atkinson, *Solid State Ionics* **2004**, *174*, 135.
- [108] Y. Meng, J. Gao, Z. Zhao, J. Amoroso, J. Tong, K. S. Brinkman, *J. Mater. Sci.* **2019**, *54*, 9291.
- [109] S. Miyoshi, Y. Akao, N. Kuwata, J. Kawamura, Y. Oyama, T. Yagi, S. Yamaguchi, *Chem. Mater.* **2014**, *26*, 5194.
- [110] B. Scherrer, M. V. F. Schlupp, D. Stender, J. Martynczuk, J. G. Grolig, H. Ma, P. Kocher, T. Lippert, M. Prestat, L. J. Gauckler, *Adv. Funct. Mater.* **2013**, *23*, 1957.
- [111] S. Ø. Stub, E. Vøllestad, T. Norby, *J. Phys. Chem. C* **2017**, *121*, 12817.
- [112] G. Gregori, M. Shirpour, J. Maier, *Adv. Funct. Mater.* **2013**, *23*, 5861.
- [113] M. Shirpour, G. Gregori, R. Merkle, J. Maier, *Phys. Chem. Chem. Phys.* **2011**, *13*, 937.
- [114] M. T. Colomer, *Adv. Mater.* **2006**, *18*, 371.
- [115] S. Wang, H. Jiang, Y. Dong, D. Clarkson, H. Zhu, C. M. Settens, Y. Ren, T. Nguyen, F. Han, W. Fan, S. Y. Kim, J. Zhang, W. Xue, S. K. Sandstrom, G. Xu, E. Tekoglu, M. Li, S. Deng, Q. Liu, S. G. Greenbaum, X. Ji, T. Gao, J. Li, *Adv. Mater.* **2022**, *34*, 2202063.
- [116] S. Hu, M. Lozada-Hidalgo, F. C. Wang, A. Mishchenko, F. Schedin, R. R. Nair, E. W. Hill, D. W. Boukhvalov, M. I. Katsnelson, R. A. W. Dryfe, I. V. Grigorieva, H. A. Wu, A. K. Geim, *Nature* **2014**, *516*, 227.
- [117] J. Zhang, A. Yang, X. Wu, J. van de Groep, P. Tang, S. Li, B. Liu, F. Shi, J. Wan, Q. Li, Y. Sun, Z. Lu, X. Zheng, G. Zhou, C.-L. Wu, S.-C. Zhang, M. L. Brongersma, J. Li, Y. Cui, *Nat. Commun.* **2018**, *9*, 5289.
- [118] C.-X. Xue, W.-H. Chen, J.-S. Liu, J.-F. Li, W.-Y. Lin, W.-E. Lin, J.-H. Wang, W.-C. Wei, T.-W. Chang, T.-C. Chang, T.-Y. Huang, H.-Y. Kao, S.-Y. Wei, Y.-C. Chiu, C.-Y. Lee, C.-C. Lo, Y.-C. King, C.-J. Lin, R.-S. Liu, C.-C. Hsieh, K.-T. Tang, M.-F. Chang, in *2019 IEEE Int. Solid-State Circuits Conf. – (ISSCC)*, IEEE, Piscataway, NJ, USA **2019**, pp. 388–390.
- [119] R. Mochida, K. Kouno, Y. Hayata, M. Nakayama, T. Ono, H. Suwa, R. Yasuhara, K. Katayama, T. Mikawa, Y. Gohou, in *2018 IEEE Symp. VLSI Technology*, IEEE, Piscataway, NJ, USA **2018**, pp. 175–176.
- [120] K. Keren, R. S. Berman, E. Buchstab, U. Sivan, E. Braun, *Science* **2003**, *302*, 1380.
- [121] C. Eckel, J. Lenz, A. Melianas, A. Salleo, R. T. Weitz, *Nano Lett.* **2022**, *22*, 973.
- [122] P. Gkoupidenis, D. A. Koutsouras, G. G. Malliaras, *Nat. Commun.* **2017**, *8*, 15448.



Mantao Huang is currently a Postdoctoral Associate in the Department of Nuclear Science and Engineering at the Massachusetts Institute of Technology, working in Professor Bilge Yildiz's research group. He received his Ph.D. degree in Materials Science and Engineering from the Massachusetts Institute of Technology in 2020. His research focuses on the development of electrochemical synapses.



Miranda Schwacke is a Ph.D. candidate in the Department of Materials Science and Engineering at the Massachusetts Institute of Technology, working in Professor Bilge Yildiz's research group. She has received her BS in Materials Science from the California Institute of Technology in 2020. During her time as an undergraduate, she pursued a variety of research projects, including studying nanoscale metallic glass with Professor Julia Greer and defects in hybrid halide perovskites at SLAC National Lab. Her Ph.D. research focus is electrochemical artificial synapses based on the intercalation of magnesium ions.



Murat Onen is a Postdoctoral Researcher at the Massachusetts Institute of Technology (MIT). He holds a Ph.D. degree in Electrical Engineering and Computer Science from the MIT. His research focuses on devices, architectures, and algorithms for analog deep learning which has led to 16 patents and numerous publications to date. Currently, he focuses on developing nanoprotonic programmable resistors and specialized training algorithms for analog crossbar accelerators.



Jesús del Alamo is Donner Professor and Professor of Electrical Engineering at the Massachusetts Institute of Technology. He holds a Ph.D. degree from the Stanford University. His research interests include compound semiconductor and novel ionic and ferroelectric devices for artificial intelligence accelerators. He has received the Intel Outstanding Researcher Award, the Semiconductor Research Corporation Technical Excellence Award, the University Researcher Award by Semiconductor Industry Association and Semiconductor Research Corporation, and the IEEE Cleo Brunetti Award. He is a Fellow of IEEE, the American Physical Society, and the Materials Research Society and a member of the Royal Spanish Academy of Engineering.



Ju Li is Battelle Energy Alliance Professor of Nuclear Science and Engineering and Professor of Materials Science and Engineering at the Massachusetts Institute of Technology. His group performs computational and experimental research on mechanical properties of materials, and energy storage and conversion. He is a Fellow of the American Physical Society, the Materials Research Society, the American Association for the Advancement of Science, and the Minerals, Metals & Materials Society.



Bilge Yildiz is Breene M. Kerr Professor in the Nuclear Science and Engineering, and the Materials Science and Engineering Departments at the Massachusetts Institute of Technology. She leads the Laboratory for Electrochemical Interfaces. Her research focuses on laying the scientific groundwork and proof-of-principle material systems for the next generation of high-efficiency devices for energy conversion and information processing, by combining experimental and computational research. Her research contributions have been recognized by the NSF CAREER, IU-MRS Somiya, the ECS Charles Tobias Young Investigator, and the Ross Coffin Purdy awards. She is a Fellow of the American Physical Society.